Monthly Notices
of the
ROYAL ASTRONOMICAL SOCIETY

MNRAS **507,** 5703–5719 (2021)
Advance Access publication 2021 August 28

https://doi.org/10.1093/mnras/stab2436

Exploring the role of cosmological shock waves in the Dianoga simulations of galaxy clusters

S. Planelles,[1,2]★ S. Borgani,[3,4,5,6] V. Quilis,[1,2] G. Murante,[3,6] V. Biffi,[6,7] E. Rasia,[3,6] K. Dolag,[7,8] G. L. Granato[3,6,9] and C. Ragone-Figueroa[3,9]

[1]*Departament d'Astronomia i Astrofísica, Universitat de València, c/ Dr. Moliner, 50, E-46100, Burjassot (Valencia), Spain*
[2]*Observatori Astronòmic, Universitat de València, E-46980 Paterna (Valencia), Spain*
[3]*INAF, Osservatorio Astronomico di Trieste, via Tiepolo 11, I-34131, Trieste, Italy*
[4]*Dipartimento di Fisica dell' Università di Trieste, Sezione di Astronomia, via Tiepolo 11, I-34131 Trieste, Italy*
[5]*INFN, Instituto Nazionale di Fisica Nucleare, Via Valerio 2, I-34127, Trieste, Italy*
[6]*IFPU, Institute for Fundamental Physics of the Universe, Via Beirut 2, I-34014 Trieste, Italy*
[7]*University Observatory Munich, Scheinerstr. 1, D-81679 Munich, Germany*
[8]*Max-Planck-Institut für Astrophysik, Karl-Schwarzschild Strasse 1, D-85748 Garching bei München, Germany*
[9]*Instituto de Astronomía Teórica y Experimental (IATE), Consejo Nacional de Investigaciones Científicas y Técnicas de la, República Argentina (CONICET) Universidad Nacional de Córdoba, Laprida 854, X5000BGR, Córdoba, Argentina*

Accepted 2021 August 13. Received 2021 August 3; in original form 2020 October 22

ABSTRACT

Cosmological shock waves are ubiquitous to cosmic structure formation and evolution. As a consequence, they play a major role in the energy distribution and thermalization of the intergalactic medium (IGM). We analyze the Mach number distribution in the Dianoga simulations of galaxy clusters performed with the SPH code GADGET-3. The simulations include the effects of radiative cooling, star formation, metal enrichment, supernova, and active galactic nuclei feedback. A grid-based shock-finding algorithm is applied in post-processing to the outputs of the simulations. This procedure allows us to explore in detail the distribution of shocked cells and their strengths as a function of cluster mass, redshift, and baryonic physics. We also pay special attention to the connection between shock waves and the cool-core/non-cool-core (CC/NCC) state and the global dynamical status of the simulated clusters. In terms of general shock statistics, we obtain a broad agreement with previous works, with weak (low-Mach number) shocks filling most of the volume and processing most of the total thermal energy flux. As a function of cluster mass, we find that massive clusters seem more efficient in thermalizing the IGM and tend to show larger external accretion shocks than less massive systems. We do not find any relevant difference between CC and NCC clusters. However, we find a mild dependence of the radial distribution of the shock Mach number on the cluster dynamical state, with disturbed systems showing stronger shocks than regular ones throughout the cluster volume.

Key words: cosmology: methods: numerical – galaxies: cluster: general – X-ray: galaxies.

1 INTRODUCTION

Cosmological shock waves play a crucial role on the formation, evolution, and thermalization of the large-scale structure (LSS) in the Universe (see Bykov, Dolag & Durret 2008; Dolag, Bykov & Diaferio 2008; Rephaeli et al. 2008, for reviews). Shocks are developed throughout the intergalactic medium (IGM) as a consequence of the hierarchical cosmic evolution. In a first phase of the evolution, the gravitational energy associated with the collapse of dark and baryonic matter is converted into kinetic energy. Most part of the gas kinetic energy gets dissipated and thermalized by shocks, thereby heating the IGM as a whole and, particularly, the intracluster medium (ICM) in virialized haloes. In the subsequent phases, the development and evolution of cosmic structures, through mergers and accretion phenomena, also produce shock waves, turbulence, and bulk gas motions, which alter the energetic balance of the intergalactic gas. Moreover, feedback associated to smaller-scale processes such as star formation, stellar winds, and supernova (SNe) explosions, or relativistic jets from active galactic nuclei (AGNs) can also create supersonic gas motions inside collapsed dark matter (DM) haloes. These hydrodynamical shocks are also responsible for transforming part of the mechanical energy released by feedback processes into thermal energy in the surrounding gas. In addition, besides the amplification of magnetic fields, these shocks, both on cosmological and galactic scales, can also accelerate particles by means of the diffusive shock acceleration mechanism (DSA; e.g. Axford, Leer & Skadron 1977; Blandford & Ostriker 1978; see also Blasi 2007 for a review), producing a population of relativistic cosmic rays (CRs) that may significantly affect gas observable properties.

Observing and studying shocks is of fundamental importance to improve our understanding of the thermalization and energetics of the LSS. Although shocks can be observed at different wavelengths, their detection is challenging. In X-ray observations, the standard

★ E-mail: susana.planelles@uv.es

© 2021 The Author(s)
Published by Oxford University Press on behalf of Royal Astronomical Society

Downloaded from https://academic.oup.com/mnras/article/507/4/5703/6359160 by Universita' di Trieste user on 13 April 2022

approach is to look for jumps in the ICM thermal quantities, such as gas density or temperature. With *Chandra*, for instance, the standard procedure is to look for jumps in surface brightness and then obtain the temperature from the spectra extracted from the regions before and after the jump. Pressure maps might be done in order to confirm what already known from gas density and temperature. However, since most of the X-ray emission comes from central cluster regions, where both gas density and temperature are high, there is not much difference between shocked and unshocked gas, making quite difficult the detection of shocks. Still, thanks to *XMM–Newton*, *Chandra,* and *Suzaku* observations, a number of merging shocks with relatively low Mach numbers ($\mathcal{M} \sim 1.5$–3) have been confirmed in several clusters (e.g. Markevitch et al. 2002, 2005; Dasadia et al. 2016). By means of high-resolution observations of the thermal Sunyaev-Zel'dovich effect (Sunyaev & Zel'dovich 1980), pressure jumps connected to shocks have also been measured in the coma cluster ($\mathcal{M} \sim 2$; Planck Collaboration X 2013; Erler et al. 2015). ICM shocks can also be detected at radio wavelengths. In this energy band, CR electrons can be accelerated or reaccelerated by merger and accretion shocks, producing synchrotron emission, which tends to be located close to the accelerating shock (see e.g. Brüggen et al. 2012; Brunetti & Jones 2014, for reviews). In this sense, there is a clear connection between observed radio relics, usually identified in outer cluster regions, and merger shocks (e.g. Ferrari et al. 2008).

The formation and evolution of shock waves have also been extensively studied by means of cosmological simulations, grid-based (e.g. Quilis et al. 1998; Miniati et al. 2001; Ryu et al. 2003; Kang et al. 2007; Skillman et al. 2008; Vazza et al. 2009b, 2010, 2011a; Planelles & Quilis 2013; Martin-Alvarez, Planelles & Quilis 2017), particle-based (e.g. Pfrommer et al. 2006; Hoeft et al. 2008; Vazza et al. 2011a; Zhang et al. 2020), or moving-mesh simulations (Schaal & Springel 2015; Schaal et al. 2016). While most of these studies are based on non-radiative simulations (e.g. Quilis et al. 1998; Miniati et al. 2001; Ryu et al. 2003; Pfrommer et al. 2006; Hoeft et al. 2008; Skillman et al. 2008; Vazza et al. 2009b, 2010, 2011a; Schaal & Springel 2015; Ha, Ryu & Kang 2018), only a few of them are based on simulations including radiative cooling and star formation (e.g. Kang et al. 2007; Pfrommer et al. 2007; Planelles & Quilis 2013; Hong et al. 2014; Hong, Kang & Ryu 2015; Martin-Alvarez et al. 2017) or AGN feedback (e.g. Vazza, Brüggen & Gheller 2013; Vazza, Gheller & Brüggen 2014; Schaal et al. 2016). Despite the diversity of cosmological codes and the different shock-finding methodologies, these numerical works report a reasonable agreement on some general shock properties and on their distribution. In this sense, simulations agree in that shock waves can be broadly divided in internal and external shocks. In general, weak shocks, with $\mathcal{M} \sim 2$–3, are developed inside collapsed structures and play a crucial role in the thermalization process of haloes; for this reason, they are often referred to as 'internal' shocks in the literature.[1] Indeed, these internal shocks are the main responsible for the energy dissipation in the Universe. On the other hand, the thermal history of galaxy clusters at large scales is controlled by the accretion of material on to DM potential wells and the exchange of gravitational energy into gas thermal energy. This process takes place through the heating of the gas by stronger (external) accretion shocks, with $\mathcal{M} \sim 10$–100, developed in the outskirts of clusters and around filaments. Given that the position of these accretion shocks results from the collision of internal and external shocks (Zhang et al. 2020), both kinds of shocks contribute to the total kinetic energy deposited in the medium. Numerical simulations, however, tend to produce significant differences in some quantities related to the injection of CRs by DSA mechanisms, limiting our current understanding on this process. In this regard, although the dynamical contribution of CRs is usually addressed in post-processing, there have been some attempts to self-consistently include this contribution in cosmological simulations (e.g. Pfrommer et al. 2006, 2007; Pfrommer, Enßlin & Springel 2008; Vazza et al. 2016). Besides, some authors have also reported some divergences in the shock patterns when comparing results from grid-based and particle-based simulations (e.g. Vazza et al. 2011a).

Therefore, a current challenge for present cosmological simulations is to be able to, consistently, understand and simulate the complex interaction between gravitational and astrophysical processes at play in the formation and evolution of cosmic structures from the smallest to the largest cosmological scales (e.g. Planelles, Schleicher & Bykov 2015, for a review). In this work, we analyze the distribution of shocks, mainly accretion shocks, in the Dianoga simulations (see also Bassini et al. 2020), a set of zoom-in cosmological hydrodynamical simulations of galaxy clusters performed with the SPH code GADGET-3. These simulations account for the effects of radiative cooling, star formation, SNe, and AGN feedback. The results obtained from the analysis of these simulations have shown a satisfactory agreement with a number of cluster observations, such as the X-ray and SZ scaling relations (Planelles et al. 2017; Truong et al. 2018), the distribution of metals (e.g. Biffi et al. 2017, 2018; Truong et al. 2019), or the thermal and chemodynamical properties of cool-core (CC) and non-cool-core (NCC) clusters (Rasia et al. 2015). Specifically, we will employ these simulations to explore in detail the distribution of shock strengths as a function of cluster mass, redshift, and feedback processes. We will also pay special attention to the connection between the Mach number distribution and the dynamical and cool-coreness state of clusters.

The paper is organized as follows. In Section 2, we describe the numerical details of this analysis, i.e. the main properties of the Dianoga simulations analyzed in this work, the shock-finding algorithm employed, and the specific numerical procedure we have followed in this study. Section 3 reports the results obtained on the global Mach number distribution in our simulations and on the connection between cluster properties and cosmic shock waves. Finally, we summarize and discuss our findings in Section 4. For the sake of completeness, in Appendix A we discuss the dependence of our results on the grid resolution, in Appendix B we analyze in more detail the connection between the distribution of shock waves and the dynamical and cool-coreness state of the clusters, and, finally, in Appendix C we explore the dependence of our results on the baryonic physics included in the simulations.

2 NUMERICAL DETAILS

In this section, we briefly introduce the main properties of the cosmological simulations to be analyzed, a brief description of the employed shock-finding algorithm, and the details of the particular numerical procedure adopted to obtain the distribution of shock waves.

[1]Although it is not strictly correct, it is quite common in the literature to indistinctly refer to internal (external) shocks as weak (strong) shocks, since most of the shocks developed within collapse structures have lower Mach numbers than external ones.

Downloaded from https://academic.oup.com/mnras/article/507/4/5703/6359160 by Universita' di Trieste user on 13 April 2022

2.1 Cosmological simulations and cluster sample

The Dianoga set of simulations analyzed in this work has been performed with an improved version of the TreePM-SPH code GADGET-3 (Springel 2005). This version of the code includes an updated hydrodynamical scheme that has been shown to ameliorate the performance of standard SPH algorithms in a number of issues (see Beck et al. 2016a, for details). Here, we provide only a brief description of the simulations, while we defer the interested reader to previous works where different aspects of the same set of simulations were investigated (Rasia et al. 2015; Villaescusa-Navarro et al. 2016; Planelles et al. 2017; Biffi et al. 2017, 2018; Ragone-Figueroa et al. 2018; Truong et al. 2018, 2019).

The set of simulations consists in re-simulations of 29 Lagrangian regions extracted from a larger parent DM-only simulation (see Bonafede et al. 2011, for details on the initial conditions). The 29 regions were identified at $z = 0$ around 29 massive DM haloes with M_{200}[2]$\sim$ 1–30 $\times\ 10^{14} h^{-1}\ \mathrm{M}_{\odot}$. Each of the low-resolution regions has been re-simulated at a finer resolution and by incorporating the baryonic component (see Planelles et al. 2013, for details). The simulations are based on a flat ΛCDM cosmology with $\Omega_{\mathrm{m}} = 0.24$, $\Omega_{\mathrm{b}} = 0.04$, $H_0 = 72$ km s^{-1} Mpc^{-1}, $\sigma_8 = 0.8$, and $n_{\mathrm{s}} = 0.96$. For the Dianoga simulations analyzed in this paper, the mass resolution for the DM (gas) particles is $m_{\mathrm{DM}} = 8.44 \times 10^8\ \mathrm{M}_{\odot}$ ($m_{\mathrm{gas}} = 1.53 \times 10^8\ \mathrm{M}_{\odot}$). In the high-resolution region, the gravitational force is computed with a Plummer-equivalent softening length of $\epsilon = 3.75\, h^{-1}$ kpc for DM and gas and $\epsilon = 2\, h^{-1}$ kpc for black hole and stellar particles.

These simulations have been run with three different prescriptions for the physics of baryons. The most complete version of these simulations, labelled as AGN, accounts for the effects of a number of gas physical processes such as gas radiative cooling, star formation, SNe feedback, metal enrichment, and a novel AGN feedback scheme that accounts for both cold and hot gas accretion on to supermassive black holes (Steinborn et al. 2015). There are two additional sets of simulations that differ only with the AGN runs in the baryonic physics they include: the NR runs, which account for only non-radiative physics, and the CSF runs, which are like the AGN ones but without including the effect of AGN feedback.

In the following, unless otherwise specified, we will consider the AGN simulation as our reference set. The set of AGN cosmological simulations has been shown to be extremely successful in reproducing some of the main observational cluster properties. These simulations have produced, for the first time and for a statistically significant cluster sample, the CC/NCC dichotomy according to thermal and chemical cluster core properties (see Rasia et al. 2015). They have also shown an excellent agreement with cluster observations in terms of the X-ray and SZ scaling relations (both at low and high redshifts; Planelles et al. 2017; Truong et al. 2018); the amount of hosted neutral hydrogen (Villaescusa-Navarro et al. 2016); the distribution of thermodynamical properties such as entropy, thermal pressure, and temperature (Rasia et al. 2015; Planelles et al. 2017); the level of mass bias and hydrostatic equilibrium (Biffi et al. 2016); or the ICM chemical enrichment distribution (Biffi et al. 2017, 2018; Truong et al. 2019).

Overall, the AGN simulation comprises a sample of $\sim$100 clusters and groups with $M_{500} > 3 \times 10^{13} h^{-1} M_{\odot}$ at $z = 0$. However, in this work we will consider only the sample of the main 29 central haloes at $z = 0$, that is, 24 clusters with $M_{200} > 8 \times 10^{14} h^{-1} \mathrm{M}_{\odot}$ and five isolated groups with M_{200} in the range of $1{-}4 \times 10^{14} h^{-1} \mathrm{M}_{\odot}$.

As described in Rasia et al. (2015), according to the core thermal properties of the clusters, the main 29 objects in the AGN simulations were classified, at $z = 0$, in CC and NCC systems. In particular, those systems with a central entropy $K_0 < 60$ keV cm^2 and a pseudo-entropy $\sigma < 0.55$ were considered as CCs, whereas those systems not fulfilling these conditions were instead classified as NCCs. In this way, 11 out of 29 haloes are classified as CC clusters. The samples of CC and NCC clusters have been shown to be different in terms of metallicity and thermodynamical profiles, showing a remarkably consistency with observations of these two cluster populations. In a similar way, based on the global dynamical state of the 29 main systems in the AGN simulations, we have classified them in six regular, eight disturbed, and 15 intermediate systems (e.g. Biffi et al. 2016; Planelles et al. 2017). In order to do this classification, we have considered a system to be regular when $\delta r < 0.07$ and $f_{\mathrm{sub}} < 0.1$, where δr and f_{sub} represent, respectively, the centre shift between the cluster minimum potential and the cluster centre of mass, in units of its radius R_{200}, and the mass fraction contributed by substructures within the same radius. Systems with larger values for both δr and f_{sub} are classified as disturbed, whereas those systems not satisfying concurrently both criteria are labelled as intermediate cases. The samples of dynamically regular and disturbed systems have been also shown to differ in terms of the levels of hydrostatic equilibrium and gas clumpiness, especially in outer cluster regions (see Biffi et al. 2016; Planelles et al. 2017, for further details).

Note that the classification of clusters in dynamically regular or disturbed depends on the radius at which the dynamical state is defined (e.g. De Luca et al. 2021, and references therein). Therefore, although the choice of this radius is quite arbitrary, it is important to keep this aspect in mind when discussing our results about the subsamples of dynamically regular and disturbed systems.

2.2 Shock-finding algorithm

In general, the development of a shock in a cosmological simulation generates a discontinuity in all the hydrodynamical gas quantities (namely, gas density, temperature, pressure, and entropy). The pre- and post-shock values of these quantities are connected to the strength of the shock through the Mach number, $\mathcal{M} = v_{\mathrm{s}}/c_{\mathrm{s}}$, where v_{s} and c_{s} are the shock speed and the sound speed ahead of the shock, respectively.

Numerical methods developed to identify hydrodynamical shocks in cosmological simulations commonly rely on the Rankine–Hugoniot jump conditions (Landau & Lifshitz 1966), which provide all the necessary information to calculate the shock Mach number. However, depending on the particular quantity and the particular way in which these conditions are applied, a number of shock-finding algorithms have been suggested. Thus, attending to the particular jump condition from which the shock Mach number is ultimately derived, there are methods based on the temperature, the density, the entropy, or the velocity jump condition (e.g. Vazza, Brunetti & Gheller 2009a). Likewise, depending on the way in which the direction of shock propagation is defined, there are two main numerical approaches: the coordinate or directional-splitting methods that follow the jump in a given hydrodynamical quantity along the coordinate axes of the computational domain (e.g. Ryu et al. 2003; Vazza et al. 2009b; Planelles & Quilis 2013; Hong et al. 2014, 2015), and the methods based on the local temperature or pressure gradients (e.g. Skillman et al. 2008; Schaal & Springel

[2] M_{Δ} is the mass within R_{Δ}, which is the radius of a sphere enclosing an average density equal to Δ times the critical cosmic density, $\rho_c(z)$. In the following, we will refer to the virial overdensity (Bryan & Norman 1998), that is $\Delta_{\mathrm{vir}} \simeq 93$ at $z = 0$ for our cosmology, or to $\Delta = 180, 200, 500, 2500$.

Downloaded from https://academic.oup.com/mnras/article/507/4/5703/6359160 by Universita' di Trieste user on 13 April 2022

2015; Schaal et al. 2016; Beck, Dolag & Donnert 2016b). Despite the obvious and unavoidable deviations between different shock-finding schemes and the distinct nature and properties of the cosmological simulations on which they are applied, all algorithms tend to produce similar properties of the shock waves in the LSS (see e.g. Vazza et al. 2011a, for a comparison study with different cosmological codes).

In this work, in order to analyze the distribution, the evolution, and the strength of shock waves in the simulations described in Section 2.1, we will employ the shock-finding algorithm presented in Planelles & Quilis (2013) (see also Martin-Alvarez et al. 2017, for further details). The definition of cells for these Lagrangian simulations will be described in Section 2.3. Here, we outline only the main procedure of the algorithm and defer the interested reader to the previous references for further details.

The shock finder algorithm presented in Planelles & Quilis (2013) was developed to measure the strength of shocks in grid-based cosmological simulations. The code relies on a directional-splitting approach along the three coordinate axes and evaluates the shock Mach number from the temperature jump equation:

$$\frac{T_1}{T_2} = \frac{(5\mathcal{M}^2 - 1)(\mathcal{M}^2 + 3)}{16\mathcal{M}^2}, \tag{1}$$

where T_1 and T_2 refer to the pre- and post-shock temperatures.

In our scheme, we first mark grid cells as *tentative shocked* if they fulfil the following conditions:

$$\text{(i)}\ \nabla \cdot \mathbf{v} < 0\,;\ \text{(ii)}\ \nabla T \cdot \nabla S > 0, \tag{2}$$

where (i) ensures the local gas velocity field $\mathbf{v}$ to be convergent and (ii) guarantees the same direction for the gradients of gas temperature T and entropy S. Then, among all the tentative shocked cells, the cell where $\nabla \cdot \mathbf{v}$ is minimum is identified as the first shock centre. Moving outwards from the shock centre, we define the extension of the shock along each of the three coordinate axes by looking for adjacent tentative shocked cells where the pre- and post-shock temperature and density satisfy $T_2 > T_1$ and $\rho_2 > \rho_1$. Once the furthest shocked cells ahead (pre-shock) and behind (post-shock) of the shock centre along each coordinate axis are identified, the Mach number along each coordinate direction is computed substituting the corresponding temperatures T_1 and T_2 in equation (1). Following this approach, shock discontinuities are spread, typically, over a few cells. The Mach numbers obtained along the three coordinate directions are then combined to get the final strength of the first shocked cell: $\mathcal{M} = (\mathcal{M}_x^2 + \mathcal{M}_y^2 + \mathcal{M}_z^2)^{1/2}$, thus minimizing projection effects in case of diagonal shocks. After this step, this shocked cell is removed from the list of tentative shocked cells. Then, the whole process is iteratively repeated focusing on the cell with the minimum value of $\nabla \cdot \mathbf{v}$.

With this procedure, we can identify all the shocked cells within the computational volume, obtaining their Mach number and the typical shock surfaces associated to cosmological shock waves. As an additional condition, in order to prevent noisy shock regions, it is a common practice to neglect all shocked cells with a Mach number lower than 1.3 (e.g. Ryu et al. 2003; Planelles & Quilis 2013; Schaal & Springel 2015).

The Rankine–Hugoniot jump conditions also provide an estimation of the amount of kinetic energy flux crossing a shock ($f_{\rm K}$) converted into thermal energy flux ($f_{\rm th}$) in the post-shock region.[3] The incoming kinetic energy flux at a shock is given by $f_K = \frac{1}{2}\rho_1(c_{s,1}\mathcal{M})^3$, where ρ_1 and $c_{s,1}$ are the gas density and the sound speed in the pre-shock region, respectively. Written in this way, $f_{\rm K}$ has units of energy flux that is energy per unit time and per unit area. Therefore, the kinetic energy flux across shock surfaces could be computed as $F_{\rm K} = f_{\rm K}(\Delta x)^2$, being Δx the spatial grid resolution. Given the kinetic energy flux, the generated thermal energy flux can be estimated as follows:

$$f_{\rm th} = \delta(\mathcal{M}) f_{\rm K}, \tag{3}$$

where $\delta(\mathcal{M})$ is the gas thermalization efficiency at shocks. Following Kang et al. (2007) for the case without a pre-existing CR component, $\delta(\mathcal{M})$ can be computed as a function of the Mach number:

$$\delta(\mathcal{M}) = \frac{2}{\gamma(\gamma-1)\mathcal{M}^2 R}\left[\frac{2\gamma\mathcal{M}^2 - (\gamma-1)}{(\gamma+1)} - R^{\gamma}\right], \tag{4}$$

where γ is the adiabatic exponent and R depends on the jump in density:

$$R \equiv \frac{\rho_2}{\rho_1} = \frac{\gamma+1}{\gamma - 1 + 2/\mathcal{M}^2}. \tag{5}$$

Besides gas thermalization, part of the energy flux at a shock can also be transferred into CRs. Indeed, by means of the DSA mechanism, CRs can also be accelerated and injected at shocks. The efficiency of this injection depends on the shock Mach number, on the degree of Alfvén turbulence, and on the direction of the magnetic field relative to the shock surface. Kang et al. (2007) inferred limits for the efficiency of CR acceleration, $\eta(\mathcal{M})$, providing fitting functions for the cases with and without a pre-existing CR component. In our analysis, once shocks are identified, we will use these fitting formulae for the case without a pre-existing CR component to estimate the flux of energy transferred into CRs:

$$f_{\rm CR} = \eta(\mathcal{M}) f_K. \tag{6}$$

Note that the treatment of energy dissipation at shocks by means of an approximated post-processing approach, like the one described above, presents a number of simplifications and caveats. However, it will allow us to get some upper limits for the efficiency of energy dissipation at shocks. It is also important to keep in mind that the Rankine–Hugoniot jump conditions provide a description of the strength of shock waves in the case of ideal shocks. Since shocks in simulations are far from being ideal, any numerical procedure based on these equations will suffer from inevitable uncertainties.

2.3 Numerical procedure

Given the characteristics of our shock-finder algorithm, in order to obtain the distribution of shock waves and their associated Mach numbers, the code needs to be applied on to a computational grid where the gas main quantities are stored in cells of any given resolution. Therefore, before running the shock finder we need to convert all the information provided by our simulations from the distribution of particles to a proper computational grid. In order to compute the Mach number within different radial apertures from the cluster centre, we proceed in the following way. For each selected simulated cluster, with virial radius $R_{\rm vir}$, we build a cubic box, with centre coinciding with the cluster centre and with a side length of $8 \times R_{\rm vir}$. The box is then discretized with a given number of cubical cells ($N = 128^3, 256^3, 512^3$ cells). On average, for the whole sample of 29 clusters in the AGN run at $z = 0$, when we consider a number of grid cells equal to $N = 128^3, 256^3$, and 512^3, we obtain a mean spatial resolution of $\Delta x \simeq 144$, 72, and 36 h^{-1} kpc, respectively. Then, we select all the gas particles within a distance of $4 \times R_{\rm vir}$ from the halo centre

[3]Note that conversion of kinetic to thermal energy at shocks in SPH simulations is described by the prescription of artificial viscosity, which not necessarily coincides with the Rankine–Hugoniot jump conditions.

Downloaded from https://academic.oup.com/mnras/article/507/4/5703/6359160 by Universita' di Trieste user on 13 April 2022

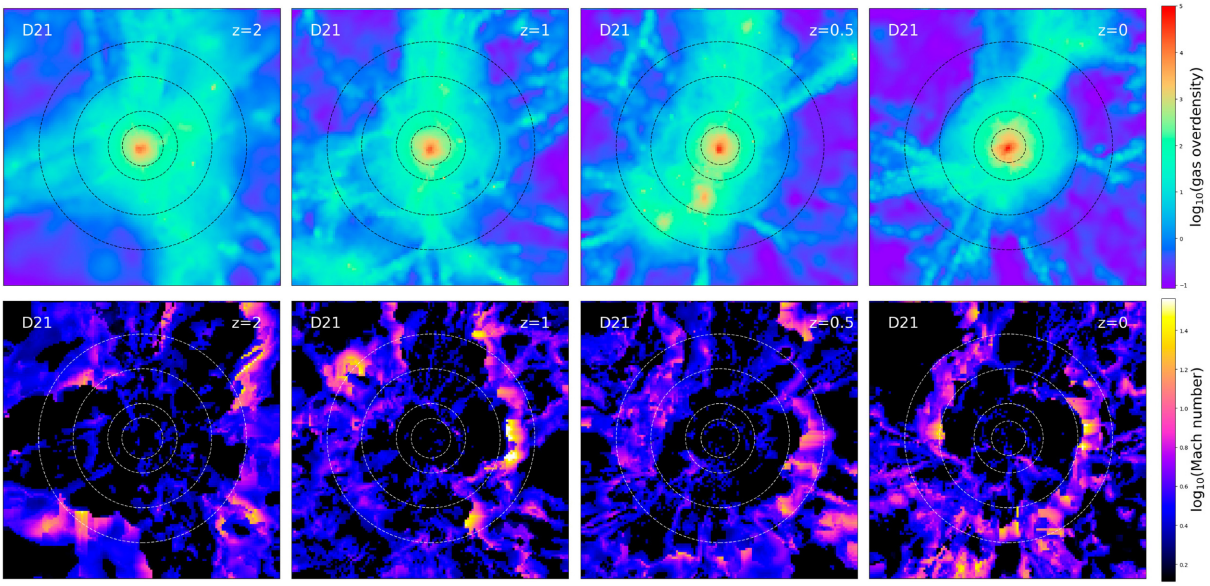


Figure 1. 2D projections of the gas overdensity (upper panels) and the Mach number distribution (lower panels) around one of the most massive clusters in our sample at different redshifts. Panels from left to right show the projections at $z = 2$, 1, 0.5, and 0, respectively. Each map, projected along the z-axis, has a length of $8 \times R_{\rm vir}$ at each redshift and a projection depth of seven cells centred on the cluster position. Circles on the maps represent R_{500}, $R_{\rm vir}$, $2 \times R_{\rm vir}$, and $3 \times R_{\rm vir}$ of the central cluster, respectively.

and we interpolate the main gas properties on to the regular grid (see Röttgers & Arth 2018, for a recent comparison of different smoothing methods) by spreading them accordingly to the same Wendland C4 kernel used for the SPH computations in the simulations (see Beck et al. 2016a). After this, we apply the shock finder in order to compute the shock Mach number for several radial apertures from the cluster centre. In particular, for each halo we have considered four different radial apertures: $R_{\rm core} \equiv 0.05 \times R_{180}$, R_{2500}, R_{500}, and $R_{\rm vir}$, although throughout this work we will mainly focus on R_{500} and $R_{\rm vir}$. Once this procedure is applied to the main 29 clusters, we analyze the distribution of shock Mach numbers as a function of redshift, cluster mass, cluster cool-coreness, cluster dynamical state, radial aperture, spatial grid resolution, and physics included in the simulations.

Unless otherwise specified, in the following we will employ as our reference results those obtained for the AGN simulations when smoothing each computational domain on to a regular grid with 128^3 cells. In Appendix A, we explore the effects of grid resolution on our results and we justify our choice. The selected spatial grid resolution is in line with the resolution employed in some recent works on the topic (e.g. Vazza et al. 2010, 2011a, 2013).

3 RESULTS

In Sections 3.1 and 3.2, we present a global analysis of different shock statistics as obtained for the whole sample of 29 regions in the AGN simulation at our reference grid resolution. We also analyze the dependence of the different quantities on cluster mass and redshift. In contrast, in Appendix B we focus our analysis on a selected subsample of six simulated clusters and we put special emphasis on the connection between shock waves and the cluster cool-coreness and dynamical state.

3.1 Global shock cell distribution

We start by analyzing the global shock cell distribution around D21, one of the most massive clusters in our AGN simulation. Fig. 1 shows 2D projections along the z-axis of the gas overdensity (upper panels) and the Mach number distribution (lower panels) at different redshifts (panels from left to right show the projections at $z = 2$, 1, 0.5, and 0, respectively). Each map has an extent of $8 \times R_{\rm vir}$ at each redshift and a projection depth of seven cells centred on the cluster position. Cluster D21, with $M_{\rm vir} = 14.26 \times 10^{14}\, h^{-1}\, {\rm M}_{\odot}$ and $R_{\rm vir} = 2.37\, h^{-1}$ Mpc, has been classified as dynamically relaxed and it is a CC cluster. As can be seen in the density maps, the cluster is already well identified at $z = 2$. The mean Mach number within the whole region is around $\sim$4 throughout the redshift evolution (see also Fig. B5). However, as evolution proceeds, the Mach number of shocks around the central cluster increases, developing a significant high-Mach number accretion shock around the cluster centre at $z = 0$. At the same time, as redshift decreases, the distribution of shocks becomes somewhat more volume-filling (see Fig. B5). Moreover, according to these maps, high-Mach number external shocks seem to be clearly dominant, in terms of strength and extension, over low-Mach number internal ones. To understand this behaviour, it is interesting to note that accretion shocks from voids and low-density regions on to the cosmic web are very volume-filling. In addition, as evolution proceeds void regions expand and increase their size, making the distribution of low-Mach number shocks within them to appear somewhat more diluted. Concurrently, the temperature of the gas in voids decreases, producing a significant difference between the temperature in voids and that in collapsed regions and, therefore, generating stronger shocks around collapsed structures.

In Appendix C, we compare the distribution at $z = 0$ shown in Fig. 1 for cluster D21 with the same distribution as obtained in the NR and CSF simulations (see Fig. C1). On average, the shock configurations are similar with comparable Mach numbers and locations, confirming the fact that the high-Mach number external shocks shown in Fig. 1 are indeed accretion shocks, with the exception of small differences in the Mach number distribution between the NR and the AGN simulations, as discussed more in Appendix B. As inferred from previous simulations (e.g. Schaal & Springel 2015; Schaal et al. 2016), outer accretion shocks show

Downloaded from https://academic.oup.com/mnras/article/507/4/5703/6359160 by Universita' di Trieste user on 13 April 2022

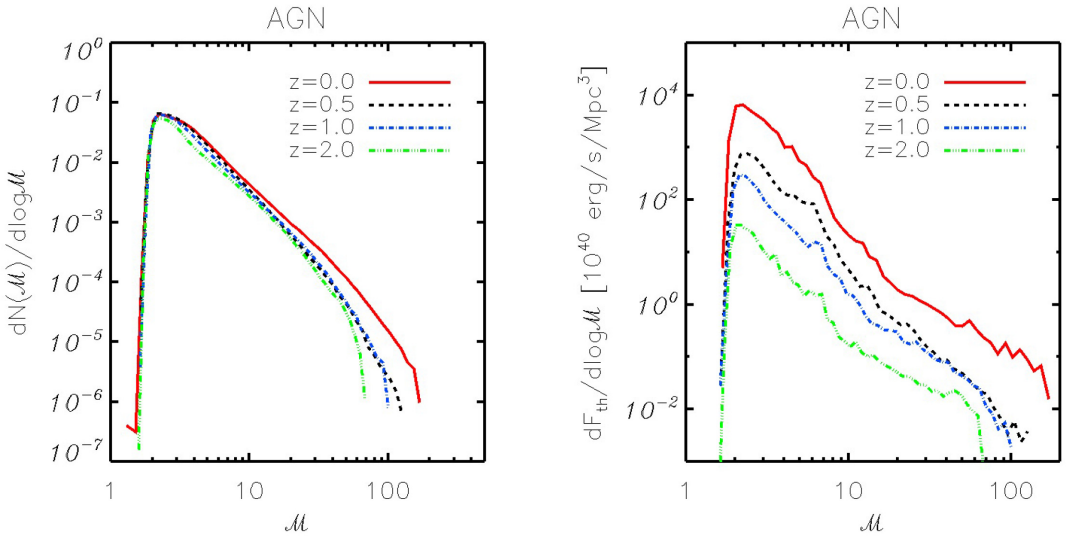


Figure 2. Left-hand panel: Mean shock cell distribution function obtained for the sample of 29 clusters in the AGN simulation as a function of redshift. Right-hand panel: Distribution of the thermal energy flux through shocks (per unit volume) for the sample of 29 clusters in the AGN simulation as a function of redshift.

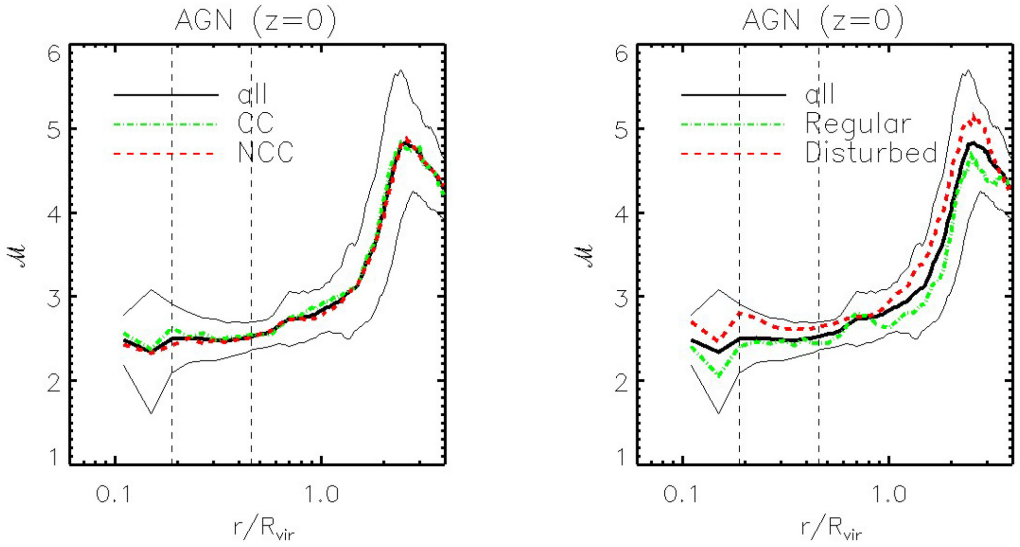


Figure 3. Volume-averaged radial profiles of the mean Mach number within $4 \times R_{\rm vir}$ for the whole sample of 29 central clusters in the AGN simulation at $z = 0$ (thick black continuous lines in both panels). Results for the subsamples of CC/NCC clusters and for the regular/disturbed clusters are shown in the left- and right-hand panels, respectively. Thin black continuous lines in both panels represent 1-σ standard deviation around the mean global profile. Dashed vertical lines stand for the mean values of R_{2500} and R_{500} as obtained for the whole sample of clusters.

typically quasi-spherical shapes and are found at distances of $\sim$1.5−2 $\times$ $R_{\rm vir}$. According to Figs 1 and C1, the accretion shock developed at $z = 0$ around cluster *D*21 also shows a quasi-spherical pattern, it wraps the LSS around the cluster, and it is located at $\sim$2.5 $\times$ $R_{\rm vir}$ from the cluster centre.

To have an idea of the way in which shocked cells of different strengths are distributed through the computational volume, in the left-hand panel of Fig. 2 we show the mean shock cell distribution function (SDF, from now on) obtained for the whole sample of 29 clusters in the AGN simulation at different redshifts. From the inspection of this figure at $z = 0$ (red continuous line), we can extract several broad conclusions. As shown in previous studies (e.g. Skillman et al. 2008; Vazza et al. 2009b; Planelles & Quilis 2013), on average most of the computational volume is filled with low-Mach number shocks ($\mathcal{M} \lesssim 3$, blue–violet colours in Fig. 1), which tend to be located within the virial radius. In contrast, stronger shocks with higher Mach numbers (orange–yellow colours in Fig. 1) are less numerous and tend to be found in outer cluster regions (see also Fig. 3). According to this behaviour, the SDF shows a peak at around $\mathcal{M} \sim 2$ and decreases beyond that value. As already discussed by some other authors (e.g. Ryu et al. 2003), internal shocks within clusters result from a number of processes such as substructure mergers, accretion of warm hot gas along filaments, or internal turbulent flow motions. On the contrary, external shocks around clusters are associated to large-scale accretion phenomena, especially when the cold gas from lower-density regions accretes on to the hot ICM. The contrast, in terms of density and temperature, between shocked and unshocked regions within the different environments

Downloaded from https://academic.oup.com/mnras/article/507/4/5703/6359160 by Universita' di Trieste user on 13 April 2022

where internal and external shocks are developed makes them to have very different strengths.

As for the dependence of the SDF on redshift, we show that the general shape of the mean SDF remains quite stable already from $z = 2$. However, the amount of shocked cells within the computational domain slightly increases with decreasing redshift, reaching a mean fraction of shocked cells of ∼13 per cent at $z = 0$. In this sense, as the redshift decreases, the number of shocked cells within the considered regions augments, giving raise, however, to a mild increase in the amount of weak internal shocks. In a similar way, as the cosmic evolution proceeds, the temperature of the IGM, especially in low-density regions, decreases, explaining the increasing high-Mach number end of the SDF (e.g. Vazza et al. 2009b; Schaal & Springel 2015; Schaal et al. 2016).

For completeness, the right-hand panel of Fig. 2 shows the mean z-evolution of the distribution of the thermal energy flux through shocks for the sample of 29 clusters in the AGN simulation. Overall, at any redshift, the maximum of the gas thermalization by shocks is found at $\mathcal{M} \sim 2$, consistent with previous studies (e.g. Ryu et al. 2003; Pfrommer et al. 2006; Skillman et al. 2008; Vazza et al. 2009b). In addition, independently of the considered redshift, the shape of the thermal energy distribution is quite alike, showing a steep negative dependence with the Mach number. In broad agreement with previous results (e.g. Pfrommer et al. 2007; Vazza et al. 2009b), we find the slope of this distribution to be within $\alpha \simeq -4$ ($z = 0$) and $\alpha \simeq -3$ ($z = 2$). Despite the high Mach number of external shocks, given the low-density environment where they are usually developed, the associated kinetic energy flux is very small, making them energetically less important. On the contrary, low-Mach number shocks, mainly developed within collapsed and denser structures, have larger values of f_K and, therefore, they are more relevant in thermalizing the ICM and producing CRs. As a consequence, most of the total thermal energy flux is processed by shocks with relatively low Mach numbers ($\mathcal{M} \lesssim 10$; e.g. Vazza et al. 2011a).

In order to explore the radial distribution of shocks around the main clusters of each simulated region, Fig. 3 shows, at $z = 0$, the averaged radial profiles of the mean Mach number for the whole sample of 29 objects in the AGN simulation (black continuous line). The mean radial profiles corresponding to the subsamples of CC/NCC and regular/disturbed systems are also shown for comparison (left- and right-hand panels, respectively).

In general, when we analyze the mean global profile, we find that the mean Mach number radial distribution is quite flat out to $\sim 0.8 \times R_{\rm vir}$, showing values within the range of ∼2.2–2.5. At radial distances above $\sim 0.8 \times R_{\rm vir}$, the profiles raise significantly, reaching values as high as $\mathcal{M} \sim 5$ in the outer cluster regions. This trend is in broad agreement with results obtained in previous studies (e.g. Vazza et al. 2009a, 2010, 2011a). In particular, Vazza et al. (2011a) performed a comparison of the radial Mach number distribution in two massive clusters as obtained with two grid-based cosmological codes and with the SPH code GADGET-3. Comparing with our results, they also found a mean Mach number value below ∼3 inside the virial radius (see also, e.g. Ha et al. 2018) and a very similar radial shock cell distribution, at least within $\sim 0.5 R_{\rm vir}$. However, beyond the virial radius, they showed that grid codes tend to identify thinner and stronger shocks than GADGET-3, producing a much sharper increase of the profiles. This abrupt rise in the strength of shocks clearly marks the transition between the outskirts of clusters and the low-density IGM. The particular shape of the profiles in these outer cluster regions could be affected by a number of factors such as the simulation numerical scheme, the specific shock-detecting approach, the different cluster environment derived from the intrinsic difference between cosmological and zoom-in simulations, or the grid resolution and/or the gas sampling procedure (especially in outer and underdense cluster regions where, by construction, SPH is not very good at sampling). For all these reasons, a precise comparison between different simulations is not straightforward. Nevertheless, even with these weaknesses, results are in comfortable agreement with those obtained using grid codes.

As for the connection between the distribution and strength of shocks and the cluster cool-coreness and global dynamical state, some previous studies attempted to analyze the relation between relaxed and unrelaxed (merging) clusters with the strength of their associated shock waves (e.g. Vazza et al. 2011b; Vazza, Roediger & Brüggen 2012). Overall, these studies found similar shock cell distributions from cluster to cluster with only small deviations connected to their particular dynamical state, especially, above the virial radius.

In our case, according to the results shown in the left-hand panel of Fig. 3, we do not obtain any difference between the mean Mach radial profiles when we look separately to the samples of CC and NCC clusters. This result is not surprising, since the classification of clusters according to their cool-coreness is based on a much smaller radial aperture ($R_{\rm core} \equiv 0.05 \times R_{180}$; Rasia et al. 2015), which is completely smoothed out at the considered resolution. As discussed in Appendix A, given the numerical approach we follow to smooth the particles' distribution on to a computational grid, it would be risky to artificially increase the spatial grid resolution to try to 'resolve' the core of clusters.

When we analyze instead the mean radial profiles obtained for the subsamples of relaxed and disturbed systems (right-hand panel of Fig. 3), we obtain a larger difference between them: disturbed clusters clearly show a higher mean Mach number than regular ones throughout the radial range. A similar behaviour was also obtained for our sample of regular and disturbed systems when we compared their degree of deviation from the hydrostatic equilibrium condition or their levels of gas clumpiness (see Biffi et al. 2016; Planelles et al. 2017, respectively). The trend shown in the right-hand panel of Fig. 3, which was somehow expected in our sample, is also in broad agreement with previous analyses (e.g. Vazza et al. 2009a).

3.2 Shock waves scaling relations

Galaxy cluster scaling relations are extremely useful to estimate cluster masses from cluster observables. In the left-hand panel of Fig. 4 we show the mean Mach number within $R_{\rm vir}$ as a function of the cluster mass M_{500} for the whole sample of 29 central clusters in the AGN simulation at redshifts $z = 0$, 0.5, 1, and 2. The value of $\mathcal{M}(< R_{\rm vir})$ is shown for the populations of dynamically regular, disturbed, and intermediate systems as specified in the legend. Moreover, CC clusters are marked with an additional circle around the main symbols, being all the clusters without this circle NCC clusters. Similarly, in the right-hand panel of Fig. 4 the mean thermal energy flux, $F_{\rm th}$, within $R_{\rm vir}$ is shown. Table 1 shows the mean values of these quantities at $z = 0$ for the different cluster samples. For the sake of completeness, the mean energy flux inverted in CR acceleration is also given.

On average, when all redshifts are considered, the mean Mach number value within the virial radius is almost flat as a function of cluster mass, with a significant dispersion for all redshifts ($\mathcal{M}(< R_{vir}) \sim [2.2, 3.8]$). However, if we consider the whole cluster sample at $z = 0$, the Pearson's correlation coefficient between the Mach number values within the virial radius and the mass M_{500} is ∼0.47, indicating a moderate correlation. Instead, when we consider

Downloaded from https://academic.oup.com/mnras/article/507/4/5703/6359160 by Universita' di Trieste user on 13 April 2022

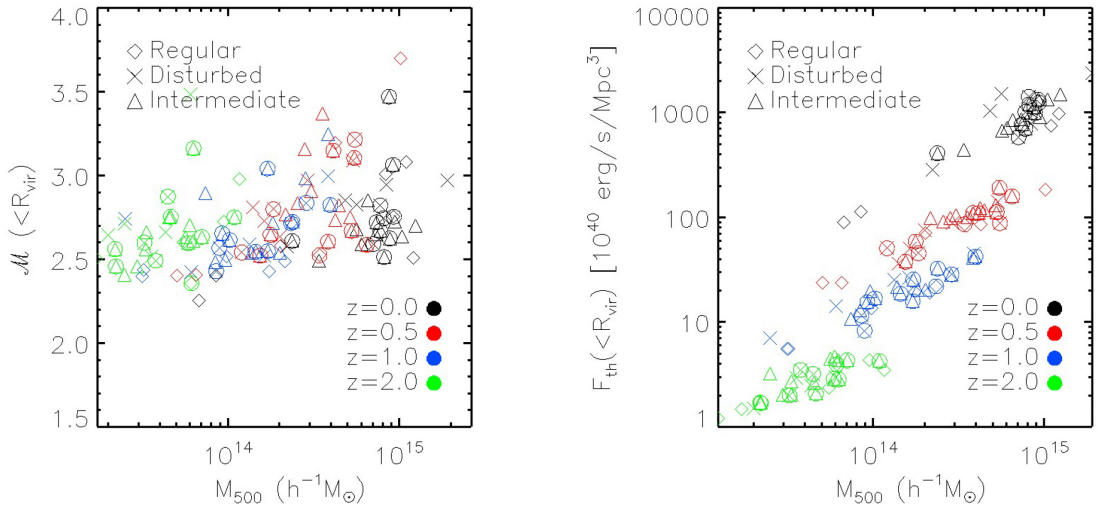


Figure 4. Left-hand panel: Mean volume-weighted Mach number within R_{vir} as a function of the cluster mass M_{500} for the whole sample of 29 central clusters in the AGN simulation at redshift $z = 0$, 0.5, 1, and 2. The value of $\mathcal{M}(< R_{vir})$ is shown for the populations of regular/disturbed/intermediate systems as specified in the legend. According to the core cluster properties, CC clusters are marked with an additional circle around the symbols shown in the legend. Right-hand panel: Same results as in the left-hand panel but for the mean thermal energy (divided by the volume of clusters), F_{th}, within R_{vir}.

Table 1. Mean values at $z = 0$ of the Mach number ($\mathcal{M}$), the thermal and the CR energy flux at shocks (F_{th} and F_{CR}, respectively) within R_{vir} for the whole sample of clusters in the AGN simulation and for the subsamples of CC/NCC and regular/disturbed systems.

Sample	$\mathcal{M}_{vir}$	$F_{th,\,vir}$ (10^{45}erg s^{-1})	$F_{CR,\,vir}$ (10^{45}erg s^{-1})
All	2.74	1.65	0.74
CC	2.78	2.77	1.25
NCC	2.71	0.96	0.43
Regular	2.67	1.15	0.44
Disturbed	2.79	2.28	1.13

the subsamples of regular and disturbed systems, we obtain a positive correlation with values of the Pearson's correlation coefficient above ∼0.7. We have checked that this trend holds from R_{200} and beyond. However, given that the considered mass range is quite narrow and the cluster sample is relatively limited, we should be cautious when deriving conclusions on this regard. As suggested by the profiles shown in Fig. 3, mild differences between dynamically regular and disturbed systems are observed throughout the radial range, contributing to a difference between the mean $\mathcal{M}(< R_{vir})$ of regular and disturbed systems, which is not found between that of CC and NCC clusters (see also Table 1).

On the contrary, as shown in the right-hand panel of Fig. 4, the mean thermal energy flux within R_{vir} shows, at fixed redshift, some correlation with cluster mass although somewhat scattered. It is only combining different redshifts that a stronger correlation shows up. However, this seems to be due to the redshift dependence. Indeed, as discussed by other authors (e.g. Ryu et al. 2003), massive galaxy clusters are supposed to represent the main sites for energy dissipation at shocks. Therefore, since the total energy processed by shocks in a simulated volume depends on the number of clusters, we should be cautious when comparing these results with preceding works (e.g. Ryu et al. 2003; Pfrommer et al. 2006; Vazza et al. 2009a). According to the results shown in Table 1, at $z = 0$ our sample of CC clusters has larger mean values of $F_{th,\,vir}$ than the NCC systems. In a similar way, as for the global dynamical state of clusters, disturbed objects show larger values of the mean thermal energy flux than regular ones. Since all these cluster subsamples have similar mean virial Mach numbers, differences could be also connected with a different amount of gas density contributing to the dissipation of energy.

Therefore, according to the global analysis of Fig. 4, our results suggest that, provided that we have a significant cluster statistics, these relations could be used as potential cluster mass proxies.

A complementary way to analyze the radial distribution of shocks around clusters is given in the left-hand panel of Fig. 5, which shows the radial shock surface distribution, out to $4 \times R_{vir}$, for the whole sample of clusters in the AGN run at $z = 0$ (black continuous line). This quantity provides an approximated estimation of the surface of shock cells, S, at their locations, r. For the sake of comparison, we also report the mean shock surface distribution obtained for the subsamples of CC/NCC and regular/disturbed systems. As shown in previous studies (Schaal & Springel 2015; Schaal et al. 2016), this distribution provides information on the location of the main shock surfaces within and around the cluster virial region and it is, therefore, very useful to estimate the position and shape of external accretion shocks. Within the virial radius, the different mean shock surface distributions show a number of peaks or bumps, which make the profiles quite irregular. These internal peaks could be connected with a number of internal shock events, such as shocks developed as a consequence of merging substructures, flow motions, or feedback processes. However, above R_{vir} all mean profiles tend to smoothly increase out to $\sim 2.5-3 \times R_{vir}$, where the curves show their maximum value. The position of this maximum could be connected with the radius (provided that accretion shocks are assumed to be spherical) of the main external accretion shock around the central clusters. It is interesting to note that there is a clear distinction between the mean shock surface distribution associated to regular and disturbed systems, with the latter showing the highest values throughout the radial range. On the contrary, we have not found such a strong dependence of $d(S/r^2)/dR$ on the clusters' core properties. Interestingly, we have obtained a moderate correlation (with a Pearson's correlation coefficient of 0.6) between the maximum value of the distribution and the mass of the associated systems. At $z = 0$, by fitting linearly the relation $\max(d(S/r^2)/dR) = f(log(M_{500}))$ (see right-hand panel of Fig. 5), we have obtained for the whole

Downloaded from https://academic.oup.com/mnras/article/507/4/5703/6359160 by Universita' di Trieste user on 13 April 2022

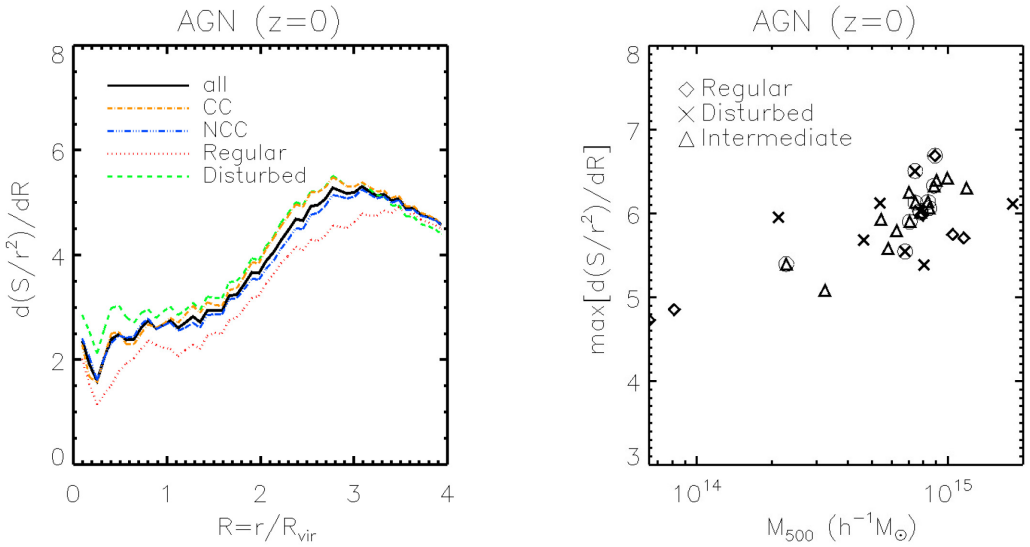


Figure 5. Left-hand panel: Mean radial shock surface distribution, out to $4 \times R_{\rm vir}$, for the whole sample of 29 clusters in the AGN simulation at $z = 0$ (black continuous line), and for the subsamples of relaxed/disturbed (red and green lines, respectively) and CC/NCC clusters (orange and blue lines). Right-hand panel: Maximum value of the radial shock surface distribution, $max(d(S/r^2)/dR$, as a function of M_{500} as obtained for the whole sample of clusters in the AGN simulation at $z = 0$. Regular, disturbed, and intermediate systems are marked according to the symbols shown in the legend, whereas CC clusters are marked with an additional circle around those symbols.

sample of clusters in the AGN run a slope $\alpha = 1.1 \pm 0.2$, although with some scatter.[4] This trend points towards a connection between the extension (or surface filling factor) of external accretion shocks developed during the collapse of structures and the mass of the final formed systems. Assuming that future observational radio facilities, such as the Square-Kilometre Array[5] (*SKA*; e.g. Acosta-Pulido et al. 2015), will be able to routinely detect large-scale shock waves, correlations like the one presented here, which is rather independent on the physics included, could become a complementary tool to estimate cluster masses (e.g. Planelles & Quilis 2013).

4 SUMMARY AND CONCLUSIONS

The formation and evolution of cosmic shock waves, inherent to cosmic structure formation and evolution processes, play a main role in the energy distribution and thermalization of the IGM. In this work, we have analyzed the distribution of these shocks in the Dianoga set of simulated galaxy clusters obtained from a set of zoom-in simulations performed with the SPH code GADGET-3. These simulations account for the effects of radiative cooling, star formation, SNe, and AGN feedback. Previous analyses of these simulations have shown an excellent agreement with a number of observed properties of the intra-cluster medium, such as the X-ray and SZ scaling relations, the metal distribution, or the thermal and dynamical properties of CC and NCC clusters (Rasia et al. 2015; Biffi et al. 2017; Planelles et al. 2017; Biffi et al. 2018; Truong et al. 2018, 2019). We have performed a further analysis of these simulations to explore in detail the distribution and evolution of the strength of shocks as a function of cluster mass, redshift, and feedback processes, paying special attention to the connection between the shock cell distribution and the cool-coreness (CC/NCC) and global dynamical state (regular/disturbed) of clusters. To perform this analysis, a grid-based shock-finding algorithm has been applied in post-processing to the outcomes of the simulations. In the following, we summarize our main findings.

(i) In general, as cluster evolution proceeds, a significant high-Mach number external accretion shock is developed around simulated clusters at $z = 0$. These outer accretion shocks show typically quasi-spherical shapes and are found at distances of $\sim(2-2.5) \times R_{\rm vir}$ from the cluster centre.

(ii) As already shown in previous works, most of the computational volume is filled with low-Mach number shocks ($\mathcal{M} \lesssim 10$), which tend to be located within the cluster boundaries, while stronger shocks with higher Mach numbers are less numerous and tend to be found in outer cluster regions.

(iii) Low-Mach number shocks, mainly developed within collapsed and dense environments, are more relevant in thermalizing the ICM and producing CRs. As a consequence, most of the total thermal energy flux is processed by relatively low-Mach number shocks ($\mathcal{M} < 10$; e.g. Vazza et al. 2011a), while stronger external shocks are energetically less important.

(iv) While the mean Mach number radial distribution within a cluster is quite flat out to $\sim 0.8 \times R_{\rm vir}$ (with mean values within $\sim$2.2–2.5), the profiles raise significantly in outer cluster regions, reaching values as high as $\mathcal{M} \sim 5$.

(v) We do not find any relevant difference between CC and NCC clusters in terms of the shock Mach number radial distribution. However, according to the clusters' dynamical state, disturbed systems tend to show stronger shocks than regular ones throughout the clusters' volume.

(vi) We find that, in general, massive clusters tend to show higher mean Mach numbers within the virial radius than less massive ones and, moreover, their associated shock waves are more efficient thermalizing the IGM. This trend is even stronger when we consider the subsamples of regular and disturbed systems.

(vii) From the analysis of the shock surface distribution function we have obtained a moderate correlation between the extension of external accretion shocks developed during the collapse of structures

[4]Similarly, we have obtained for the reduced sample of clusters in the CSF and NR simulations a value of $\alpha = 1.1 \pm 0.9$ and $\alpha = 1.3 \pm 0.9$, respectively.
[5]https://www.skatelescope.org/

Downloaded from https://academic.oup.com/mnras/article/507/4/5703/6359160 by Universita' di Trieste user on 13 April 2022

and the mass of the final formed systems (see also Appendix B). We expect this correlation, which is independent of the physics included in the simulations, to become in principle a way to infer cluster masses.

(viii) As for the redshift evolution of the shock cell distribution, we find that the fraction of cells hosting shocks in the different simulated volumes slightly increases with decreasing redshift (from ∼46 per cent at $z = 2$ out to 55–60 per cent at $z = 0$; see Appendix B). On the other hand, the mean Mach number remains quite flat for all clusters ($3 \lesssim \mathcal{M} \lesssim 4$).

(ix) As a consequence of the different radiative and feedback processes included in the NR, CSF, and AGN simulations, some differences in the distribution of shocks within the clusters' virial region are clearly detectable. On the contrary, the large-scale Mach number distribution, which is mainly driven by gravitational effects associated to cosmic structure formation, is very similar in the three sets of simulations (see Appendix C).

(x) From the analysis of the shock cell distribution function around one of the most massive clusters in our sample, we find that AGN feedback tends to produce a small shortfall of shocked cells in the range $4 \lesssim \mathcal{M} \lesssim 60$, compared to the NR run. This discrepancy is similarly present when comparing the CSF and the NR simulation, suggesting its origin to be related to the impact of radiative processes in general (see Appendix C).

Although shocks can be observed at different wavelengths, such as X-rays, millimetric (via the SZ effect) and radio, their detection is challenging. However, the key role played by shocks in the thermalization and energetics of the LSS makes mandatory observing and understanding them in detail. In this regard, it is crucial to perform detailed analyses of the formation and evolution of shocks in *realistic* and complex simulations like the ones analyzed in this project. These studies need, however, to be improved in terms of shock identification and estimation of the energy dissipation at shocks. Moreover, even when the analyzed cluster sample is perfectly suitable for the present study, larger samples are needed in order to reach more robust statistical conclusions. The combination of results from simulations with the expected observations from the next generation of X-rays, SZ, and radio instruments (see, for instance, Vazza et al. 2019) will be essential to deepen our understanding of the main properties of the LSS of the Universe.

ACKNOWLEDGEMENTS

We thank the anonymous referee for his/her constructive comments. This work has been performed under the Project HPC-EUROPA3 (INFRAIA-2016-1-730897), with the support of the EC Research Innovation Action under the H2020 Programme; in particular, SP gratefully acknowledges the hospitality of the Department of Physics of the University of Trieste and the computer resources and technical support provided by CINECA. SP and VQ acknowledge financial support from the *Spanish Ministerio de Ciencia, Innovación y Universidades* (MICINN, grant PID2019-107427GB-C33) and the Generalitat Valenciana (grant PROMETEO/2019/071). SB and ER acknowledge financial support from the PRIN-MIUR 2015W7KAWC grant and the INFN InDARK grant. VB acknowledges support by the DFG project nr. 415510302. KD acknowledges support by the Deutsche Forschungsgemeinschaft (DFG, German Research Foundation) under Germany's Excellence Strategy – EXC-2094 – 3907833 as well as the COMPLEX project from the European Research Council (ERC) under the European Union's Horizon 2020 research and innovation program grant agreement ERC-2019-AdG 860744.

DATA AVAILABILITY

The data underlying this article will be shared on reasonable request to the corresponding author.

REFERENCES

Acosta-Pulido J. A. et al., 2015, preprint (arXiv:1506.03474)
Axford W. I., Leer E., Skadron G., 1977, Int. Cosmic Ray Conf., 11, 132
Bassini L. et al., 2020, A&A, 642, A37
Beck A. M. et al., 2016a, MNRAS, 455, 2110
Beck A. M., Dolag K., Donnert J. M. F., 2016b, MNRAS, 458, 2080
Biffi V. et al., 2016, ApJ, 827, 112
Biffi V. et al., 2017, MNRAS, 468, 531
Biffi V., Planelles S., Borgani S., Rasia E., Murante G., Fabjan D., Gaspari M., 2018, MNRAS, 476, 2689
Blandford R. D., Ostriker J. P., 1978, ApJ, 221, L29
Blasi P., 2007, Nucl. Phys. B Proc. Suppl., 165, 122
Bonafede A., Dolag K., Stasyszyn F., Murante G., Borgani S., 2011, MNRAS, 418, 2234
Brüggen M., Bykov A., Ryu D., Röttgering H., 2012, Space Sci. Rev., 166, 187
Brunetti G., Jones T. W., 2014, Int. J. Mod. Phys. D, 23, 1430007
Bryan G. L., Norman M. L., 1998, ApJ, 495, 80
Bykov A. M., Dolag K., Durret F., 2008, Space Sci. Rev., 134, 119
Dasadia S. et al., 2016, ApJ, 820, L20
De Luca F., De Petris M., Yepes G., Cui W., Knebe A., Rasia E., 2021, MNRAS, 504, 5383
Dolag K., Bykov A. M., Diaferio A., 2008, Space Sci. Rev., 134, 311
Erler J., Basu K., Trasatti M., Klein U., Bertoldi F., 2015, MNRAS, 447, 2497
Ferrari C., Govoni F., Schindler S., Bykov A. M., Rephaeli Y., 2008, Space Sci. Rev., 134, 93
Ha J.-H., Ryu D., Kang H., 2018, ApJ, 857, 26
Hoeft M., Brüggen M., Yepes G., Gottlöber S., Schwope A., 2008, MNRAS, 391, 1511
Hong S. E., Ryu D., Kang H., Cen R., 2014, ApJ, 785, 133
Hong S. E., Kang H., Ryu D., 2015, ApJ, 812, 49
Kang H., Ryu D., Cen R., Ostriker J. P., 2007, ApJ, 669, 729
Landau L. D., Lifshitz E. M., 1966, Hydrodynamik. Akademie-Verlag, Berlin
Markevitch M., Gonzalez A. H., David L., Vikhlinin A., Murray S., Forman W., Jones C., Tucker W., 2002, ApJ, 567, L27
Markevitch M., Govoni F., Brunetti G., Jerius D., 2005, ApJ, 627, 733
Martin-Alvarez S., Planelles S., Quilis V., 2017, Ap&SS, 362, 91
Miniati F., Ryu D., Kang H., Jones T. W., Cen R., Ostriker J. P., 2000, ApJ, 542, 608
Miniati F., Jones T. W., Kang H., Ryu D., 2001, ApJ, 562, 233
Nelson D., Genel S., Pillepich A., Vogelsberger M., Springel V., Hernquist L., 2016, MNRAS, 460, 2881
Pfrommer C., Springel V., Enßlin T. A., Jubelgas M., 2006, MNRAS, 367, 113
Pfrommer C., Enßlin T. A., Springel V., Jubelgas M., Dolag K., 2007, MNRAS, 378, 385
Pfrommer C., Enßlin T. A., Springel V., 2008, MNRAS, 385, 1211
Planck Collaboration X, 2013, A&A, 554, A140
Planelles S., Quilis V., 2013, MNRAS, 428, 1643
Planelles S., Borgani S., Dolag K., Ettori S., Fabjan D., Murante G., Tornatore L., 2013, MNRAS, 431, 1487
Planelles S., Borgani S., Fabjan D., Killedar M., Murante G., Granato G. L., Ragone-Figueroa C., Dolag K., 2014, MNRAS, 438, 195
Planelles S., Schleicher D. R. G., Bykov A. M., 2015, Space Sci. Rev., 188, 93
Planelles S. et al., 2017, MNRAS, 467, 3827
Quilis V., Ibáñez J. M., Sáez D., 1998, ApJ, 502, 518
Ragone-Figueroa C., Granato G. L., Ferraro M. E., Murante G., Biffi V., Borgani S., Planelles S., Rasia E., 2018, MNRAS, 479, 1125
Rasia E. et al., 2015, ApJ, 813, L17
Rephaeli Y., Nevalainen J., Ohashi T., Bykov A. M., 2008, Space Sci. Rev., 134, 71
Röttgers B., Arth A., 2018, preprint (arXiv:1803.03652)

Downloaded from https://academic.oup.com/mnras/article/507/4/5703/6359160 by Universita' di Trieste user on 13 April 2022

Ryu D., Kang H., Hallman E., Jones T. W., 2003, ApJ, 593, 599
Schaal K. et al., 2016, MNRAS, 461, 4441
Schaal K., Springel V., 2015, MNRAS, 446, 3992
Skillman S. W., O'Shea B. W., Hallman E. J., Burns J. O., Norman M. L., 2008, ApJ, 689, 1063
Springel V., 2005, MNRAS, 364, 1105
Steinborn L. K., Dolag K., Hirschmann M., Prieto M. A., Remus R.-S., 2015, MNRAS, 448, 1504
Sunyaev R. A., Zel'dovich I. B., 1980, MNRAS, 190, 413
Truong N. et al., 2018, MNRAS, 474, 4089
Truong N. et al., 2019, MNRAS, 484, 2896
Vazza F., Brunetti G., Gheller C., 2009a, MNRAS, 395, 1333
Vazza F., Brunetti G., Kritsuk A., Wagner R., Gheller C., Norman M., 2009b, A&A, 504, 33
Vazza F., Brunetti G., Gheller C., Brunino R., 2010, New A, 15, 695
Vazza F., Dolag K., Ryu D., Brunetti G., Gheller C., Kang H., Pfrommer C., 2011a, MNRAS, 418, 960
Vazza F., Brunetti G., Gheller C., Brunino R., Brüggen M., 2011b, A&A, 529, A17
Vazza F., Roediger E., Brüggen M., 2012, A&A, 544, A103
Vazza F., Brüggen M., Gheller C., 2013, MNRAS, 428, 2366
Vazza F., Gheller C., Brüggen M., 2014, MNRAS, 439, 2662
Vazza F., Brüggen M., Wittor D., Gheller C., Eckert D., Stubbe M., 2016, MNRAS, 459, 70
Vazza F., Ettori S., Roncarelli M., Angelinelli M., Brüggen M., Gheller C., 2019, A&A, 627, A5
Villaescusa-Navarro F. et al., 2016, MNRAS, 456, 3553
Zhang C., Churazov E., Dolag K., Forman W. R., Zhuravleva I., 2020, MNRAS, 494, 4539

APPENDIX A: DEPENDENCE ON GRID RESOLUTION

When we smooth a distribution of SPH particles on to a grid, ideally, we want to reach a grid resolution comparable with the resolution we have in the SPH simulation. However, this is not trivial, especially when we employ a regular grid (see Röttgers & Arth 2018, for a recent analysis of different smoothing methods). Therefore, once we have smoothed a distribution of particles on to a grid, we need to make sure that, for instance, the total mass inside the considered volume is conserved. This means that we should get the same gas mass within a given region when comparing the summation over all SPH particles with the integral of the gas density over a grid. To address this issue, Fig. A1 shows the mean relative error in recovering the gas mass within different radial apertures from the cluster centre as obtained for the whole sample of 29 clusters in the AGN simulations at $z = 0$. The considered apertures are spherical regions of radius equal to 0.5, 1, 2, and 4 times the virial radius of each halo. The last tick mark on the x-axis, labelled as 'Box', stands for the volume of the whole cubical box, that is, including as well the corners of the box and not just the sphere, with side length equal to $8 \times R_{\rm vir}$. Then, the error in mass is computed as the relative difference between the mass obtained from the direct summation over the sample of particles within a given region and from the integration of the gas density smoothed out on to a grid of a given resolution, that is $(M_{\rm p} - M_{\rm grid})/M_{\rm p}$, being $M_{\rm p}$ and $M_{\rm grid}$ the masses derived from the distribution of particles and from the grid. Results are shown for three different resolutions, which correspond to discretize the considered volumes with 128^3, 256^3, and 512^3 cells (black, green, and red lines, respectively). The results shown in this figure indicate that when we consider the lowest resolution, the one corresponding to 128^3 cells, the error in mass is around $\sim$1 per cent for all the considered radial apertures. Instead, when we increase the grid resolution the error increases significantly, especially for the resolution corresponding to 512^3 cells and for radial apertures beyond $2 \times R_{\rm vir}$.

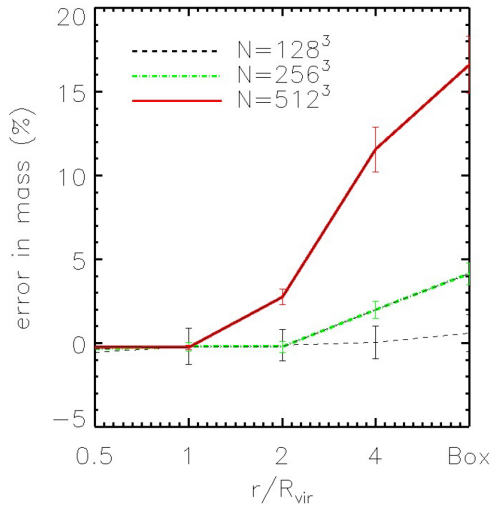


Figure A1. Mean relative error in recovering the gas mass within different radial apertures from the cluster centre as obtained for the whole sample of 29 clusters in the AGN simulations at $z = 0$. The relative error in mass is computed as $(M_{\rm p} - M_{\rm grid})/M_{\rm p}$, being $M_{\rm p}$ and $M_{\rm grid}$ the masses obtained from the distribution of particles and from the integral of the gas density over the grid. The considered radial apertures are spherical regions of radius equal to 0.5, 1, 2, and 4 times the virial radius of each halo. The last tick mark on the x-axis stands for the volume of the whole cubical box with side length equal to $8 \times R_{\rm vir}$. Results are shown for the resolutions corresponding to discretizing the considered volumes with 128^3, 256^3, and 512^3 cells (black, green, and red lines, respectively). Error bars stand for $1 - \sigma$ standard deviation around each mean distribution.

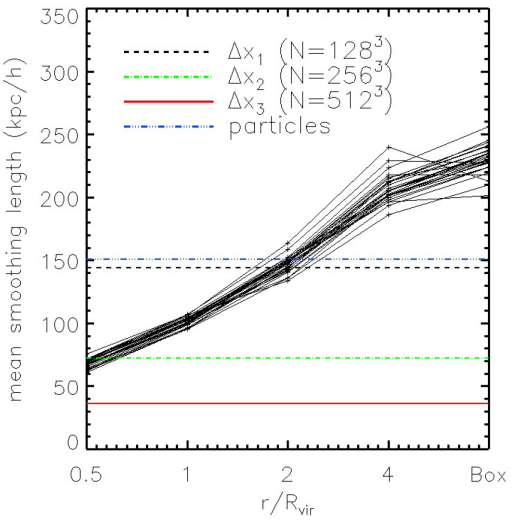


Figure A2. Distribution of the mean smoothing length of all the gas particles within different radial apertures from the cluster centre for each of the 29 main haloes in the AGN simulations at $z = 0$ (black continuous lines). The considered radial apertures are the same as those shown in Fig. A1. Horizontal lines represent the corresponding mean grid resolutions when discretizing the considered volumes with 128^3, 256^3, and 512^3 cells (horizontal black, green, and red lines, respectively). An additional horizontal blue line represents the mean smoothing length of all the gas particles within the whole simulation as obtained from the whole sample of 29 clusters.

To understand better this trend, Fig. A2 shows the distribution of the mean smoothing length of all the gas particles within different radial apertures from the cluster centre for each of the 29 main haloes in the AGN simulations at $z = 0$ (black continuous lines). As

Downloaded from https://academic.oup.com/mnras/article/507/4/5703/6359160 by Universita' di Trieste user on 13 April 2022

expected, the mean smoothing length of particles within clusters is relatively low within the virial radius ($\sim 70\,h^{-1}$kpc) and increases in outer regions ($\sim 220\,h^{-1}$kpc). As in the previous figure, we have considered spherical regions of radius equal to 0.5, 1, 2, and 4 times the virial radius of each halo. We have also considered the volume of the whole cubical box with side length equal to $8 \times R_{\rm vir}$. Horizontal lines represent the corresponding mean grid resolutions when discretizing the considered volumes with 128^3, 256^3, and 512^3 cells (horizontal black, green, and red lines, respectively). An additional horizontal blue line represents the mean smoothing length of all gas particles as obtained from the whole sample of 29 clusters. According to these results, the resolution corresponding to a grid with 128^3 cells (horizontal black line) is comparable to the mean smoothing length of all particles ($\sim 150\,h^{-1}$kpc; horizontal blue line). Although this is a simple approximation, in view of the results shown in Figs A1 and A2, we decided to adopt as our reference resolution the one corresponding to discretize the distribution of particles on to a regular grid with 128^3 cubical cells.

Early studies with grid-based cosmological codes (e.g. Kang et al. 2007) have shown that for a fixed grid resolution it is difficult to capture smaller-scale shock features, meaning that shocks in inner cluster regions may not be fully identified. In our study, we have checked that, as the spatial grid resolution is artificially increased, a larger amount of weaker and thinner shock surfaces can be identified. We should, however, take this result with caution since, as shown for the mass conservation in Fig. A1, the artificial improvement of the grid resolution can generate unrealistic and spurious identification of shocks. Therefore, trying to resolve shocks in cluster outskirts with a grid resolution higher than the actual SPH resolution may introduce significant spurious effects. Indeed, the proper way to study the effect of spatial resolution on our results would be to re-simulate the sample of 29 regions, with the same initial conditions, but with different mass resolutions. Although this option is beyond the purpose of this paper, it could be addressed in future works. Therefore, taking into account the results discussed in this section, we have chosen the resolution corresponding to $N = 128^3$ cells as our reference one throughout the paper.

APPENDIX B: CONNECTION BETWEEN SHOCKS AND GALAXY CLUSTERS

In order to analyze in more detail the connection between the distribution of shock waves and the dynamical or cool-coreness state of the clusters, in this section we will focus our analysis on a smaller selection of six systems, whose main properties are summarized in Table B1. Although this reduced sample is not statistically representative, it has been chosen in order to have systems with different masses, core, and dynamical classifications.

Fig. B1 shows projections along the z-axis of the gas overdensity and the Mach number distribution around each of the six selected cluster regions at $z = 0$ (including region D21, whose redshift evolution has been shown in Fig. 1). For the central cluster of each region, radii R_{500}, $R_{\rm vir}$, $2 \times R_{\rm vir}$, and $3 \times R_{\rm vir}$ are also shown. According to the density maps, these projections clearly show a wide variety of LSSs around the different haloes. Indeed, outside the virial radius, a complex and irregular distribution of filaments and void regions dominates the simulated volume. As expected, within the clusters' virial region the density distribution is dominated by the very central area within R_{500}, although smaller substructures are also visible in outer regions, in-between R_{500} and $R_{\rm vir}$.

Interestingly, if we look instead at the shock Mach number maps shown in Fig. B1, most of the regions show a high-Mach number shock surface (located at several virial radii from the cluster centre) wrapping the large-scale density distribution and separating the external unshocked gas from the cluster outskirts. Although the shape of these external accretion shocks is assumed to be quasi-spherical, as in region $D21$, there are some other regions, like $D3$, $D4$, or $D6$, which show a more irregular 'flower-like' distribution. Some studies have shown that this particular pattern is quite common and results from the intersection between merger and accretion shocks developed during clusters' evolution (e.g. Zhang et al. 2020). Instead, within the virial radius clusters show different and more irregular shock patterns. In some regions, like $D2$ or $D10$, some bow shocks with low-Mach number are detectable in the area within R_{500} and $R_{\rm vir}$.

Similar to Fig. 2, we show in Fig. B2 the shock cell distribution function (left-hand panel) and the differential distribution of the thermal energy flux through shocks (right-hand panel) for the reduced sample of clusters in the AGN simulation at $z = 0$. These distributions have been computed for a cubical region of side length equal to $8 \times R_{\rm vir}$ around each cluster. Obviously, for all clusters both distributions show a broad agreement with the mean trend shown in Section 3.1 for the complete sample of systems. In general, we do not distinguish any particular trend depending on the core or global dynamical state of the different clusters. However, for a fixed Mach number, the most massive clusters (i.e. D6, D10, and D21) tend to host a larger percentage of shocked cells and seem to be more efficient in thermalizing the IGM, in agreement with the results shown in Fig. 4. In addition, even though regions D6, D10, and D21 are quite similar in terms of the shock cell distribution function through most of the Mach number range, shocks within region D21 (connected to the only dynamically regular system in our sample) seem to process a lower amount of energy than shocks within regions D6 and D10,

Table B1. Main properties of the six selected clusters at $z = 0$ in the AGN run. Columns from left to right give, respectively, the cluster id, the viral mass ($M_{\rm vir}$), the virial ($R_{\rm vir}$) and R_{500} radii, the CC/NCC classification based on their core properties, the regular/disturbed/intermediate classification based on their global dynamical state, and the spatial resolution of the computational boxes built around them when we consider a box of side length equal to $8 \times R_{\rm vir}$ discretized with a number of cells equal to $N_1 = 128^3$, $N_2 = 256^3$, $N_3 = 512^3$.

Cluster	$M_{\rm vir}$ ($10^{14}\,h^{-1}\,{\rm M}_\odot$)	$R_{\rm vir}$ (h^{-1} Mpc)	R_{500} (h^{-1} Mpc)	Core state	Dynamical state	Δx_1 (h^{-1} kpc)	Δx_2 (h^{-1} kpc)	Δx_3 (h^{-1} kpc)
D2	5.26	1.70	0.74	CC	Intermediate	105.3	52.9	26.5
D3	6.53	1.83	0.84	NCC	Intermediate	113.3	56.9	28.5
D4	5.21	1.69	0.73	NCC	Disturbed	105.0	52.7	26.4
D6	15.41	2.43	1.08	NCC	Intermediate	150.8	75.7	37.9
D10	15.46	2.43	1.07	CC	Disturbed	151.1	75.9	38.0
D21	14.26	2.37	1.17	CC	Regular	146.9	73.8	37.0

Downloaded from https://academic.oup.com/mnras/article/507/4/5703/6359160 by Universita' di Trieste user on 13 April 2022

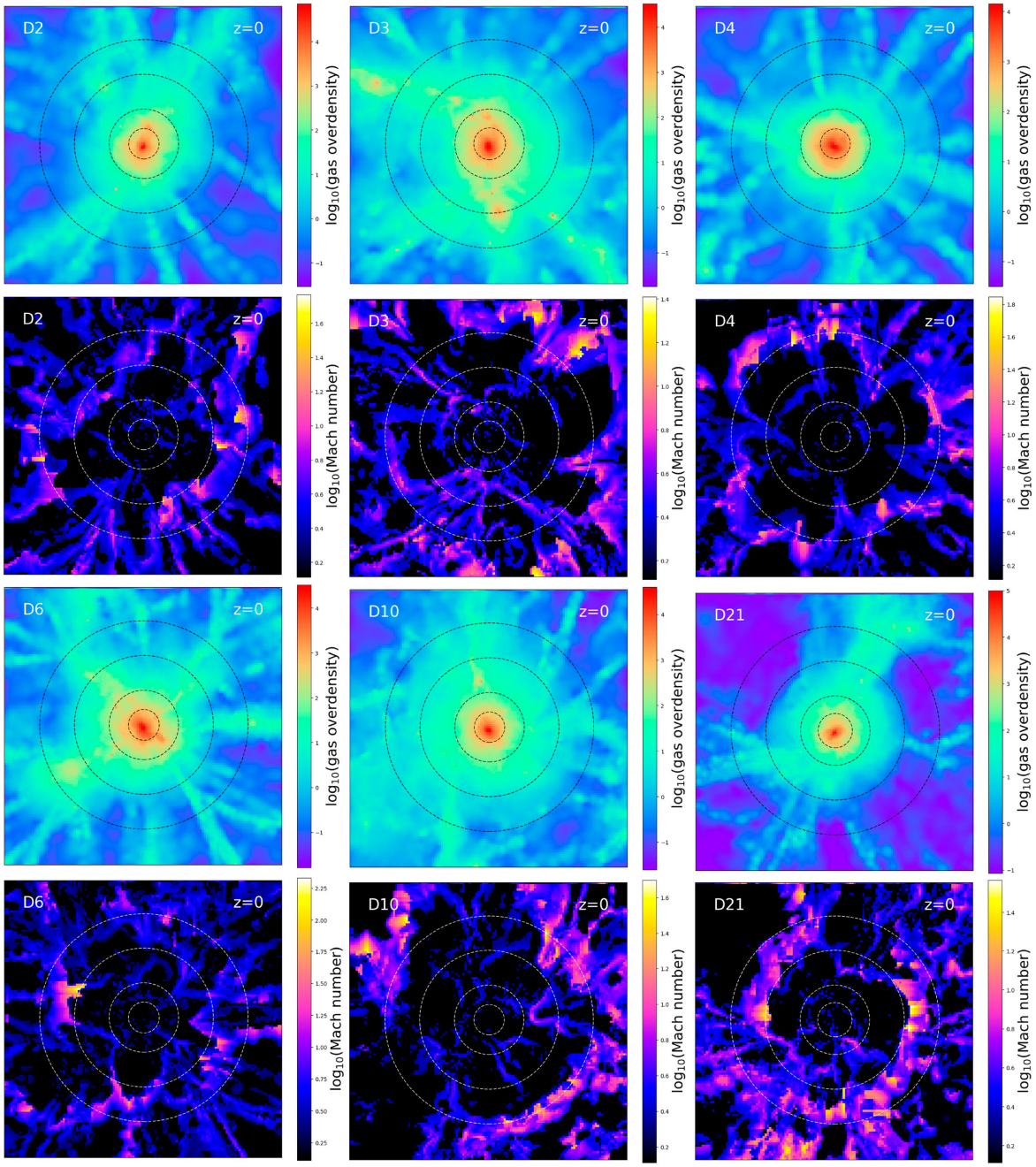


Figure B1. 2D projections of the gas overdensity and the Mach number distribution at $z = 0$ around each of the six clusters whose properties are given in Table B1. Each map, projected along the z-axis, has a side length of $8 \times R_{\rm vir}$ and a projection depth of seven cells centred on the cluster position. Circles on the maps represent R_{500}, $R_{\rm vir}$, $2 \times R_{\rm vir}$, and $3 \times R_{\rm vir}$ of the central object, respectively.

especially for $10 \lesssim \mathcal{M} \lesssim 80$. A similar trend was also obtained by Vazza et al. (2010), who found mild differences, especially for shocks with $\mathcal{M} > 10$, between their merging and relaxed cluster samples, with the relaxed systems processing $\sim$10 times less thermal energy than the merging ones.

It is also important to stress that the distributions shown in Figs 2 and B2 are derived from the 3D distribution of shocks around each cluster, while the maps are projections of a slice across the cluster centre. In this way, most of the shocks that boost the SDF at high-Mach number for region D6 are not visible from the map.

The left-hand panel of Fig. B3 reports the mean Mach number radial profiles, out to $4 \times R_{\rm vir}$, for the reduced sample of clusters at $z = 0$. Despite the different dynamical classification of the systems, they show very similar radial Mach number distributions, especially within R_{500}. Indeed, out to the viral radius, all clusters show mean Mach number values within $2 \lesssim \mathcal{M} \lesssim 3$. Above $R_{\rm vir}$ the mean strength of shocks smoothly increases, reaching values as high as $\mathcal{M} \lesssim 4$ at $2 \times R_{\rm vir}$. As discussed in Section 3.1, the shape of these profiles is in line with the results presented in previous analyses (e.g. Vazza et al. 2009a, 2010, 2011a). In our case, we do not find a

Downloaded from https://academic.oup.com/mnras/article/507/4/5703/6359160 by Universita' di Trieste user on 13 April 2022

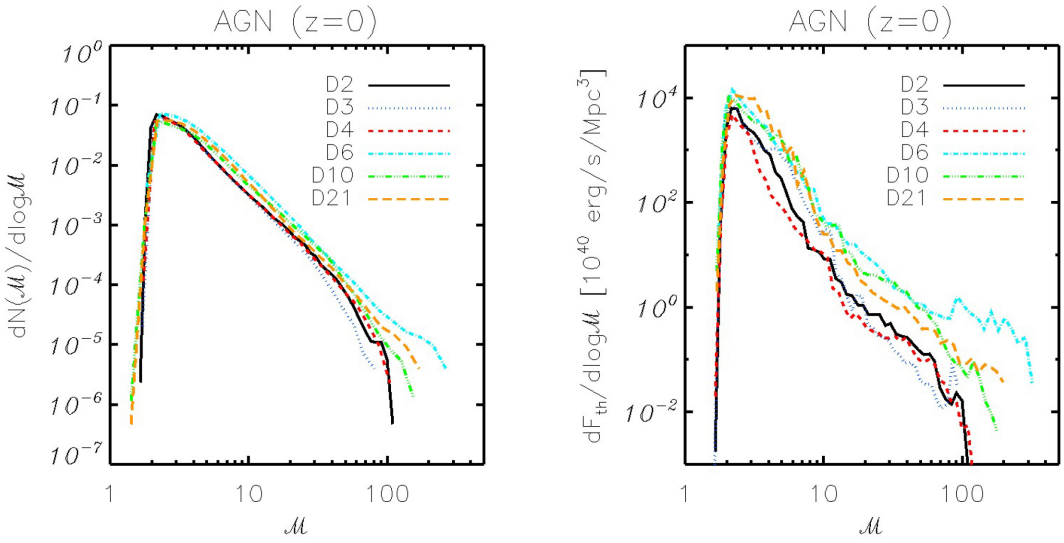


Figure B2. Left-hand panel: Shock cell distribution function for the reduced sample of clusters in the AGN simulation at $z = 0$. Right-hand panel: Differential distribution of the thermal energy through shocks (divided by the volume of each region) for the reduced sample of clusters in the AGN simulation at $z = 0$.

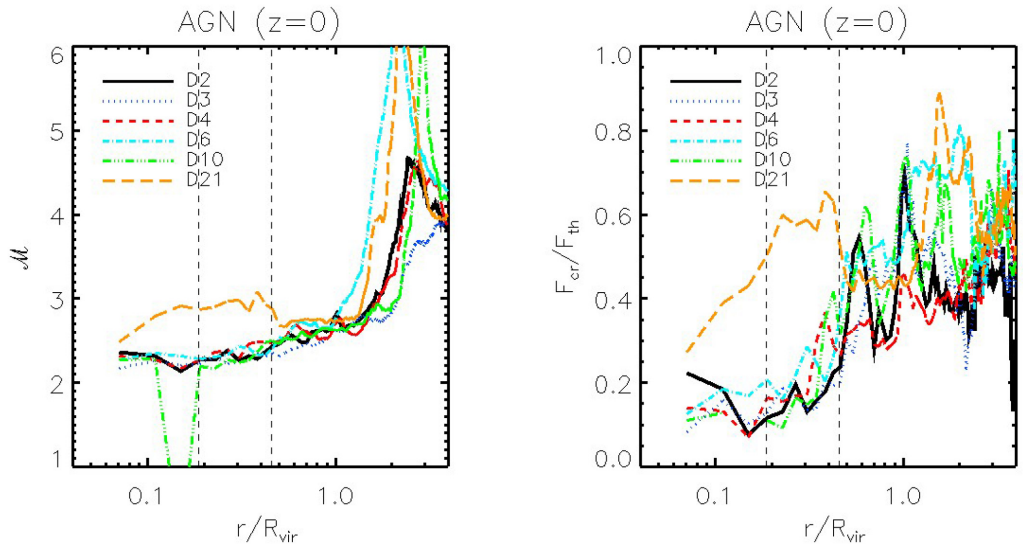


Figure B3. Left-hand panel: Volume-averaged radial profiles of the mean Mach number for the six main central clusters of regions D2, D3, D4, D6, D10, and D21 out to 4 × R_{vir}. Right-hand panel: Mean radial profiles as in the left-hand panel but for the ratio of the CR energy flux over the thermal energy flux out to 4 × R_{vir} of each cluster. Vertical lines mark the position of the mean value of radii R_{2500} and R_{500}.

clear trend depending either on the dynamical state of the clusters or on their cool-coreness. In this regard, it is interesting to remind that the classification in relaxed/disturbed systems was done within R_{200} and, therefore, it does not mean that a relaxed cluster must have a smooth gas density distribution up to ∼2–3 R_{vir}. However, we still note that at ∼2–3 R_{vir} the shock cell distributions within regions D6, D10, and D21 reach higher Mach numbers than shocks within the rest of regions.

In order to explore the global efficiency of these systems in accelerating CR at shocks, the right-hand panel of Fig. B3 shows the mean radial profiles of the ratio between the CR energy flux and the thermal energy flux, F_{CR}/F_{th}, at $z = 0$. On average, regardless of the dynamical state of the different clusters, we do not find relevant differences between them throughout the radial range. However, region D21 shows larger values than expected, especially below R_{500}. These peaks in the F_{CR}/F_{th} radial distribution must be connected with the slightly larger radial Mach number profiles shown by this system in the central regions (see left-hand panel). Leaving aside these deviations, the mean radial distribution of the ratio F_{CR}/F_{th} tends to increase with the distance from the cluster centre, providing stringent limits to the energy dissipation ratio. Although it is not possible to perform a straightforward comparison among different simulations, the obtained trend and average value of the F_{CR}/F_{th} ratio are in line with the estimates shown in previous works (see e.g. Vazza et al. 2009a, where some dependences of the F_{CR}/F_{th} ratio on the energy dissipation model employed are also shown).

As it has been shown in Fig. 5, Fig. B4 shows now the radial shock surface distribution, out to 4 × R_{vir}, for the reduced sample of clusters

Downloaded from https://academic.oup.com/mnras/article/507/4/5703/6359160 by Universita' di Trieste user on 13 April 2022

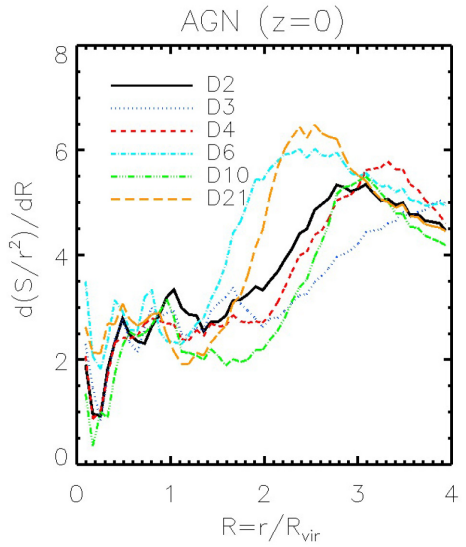


Figure B4. Radial shock surface distribution out to $4 \times R_{\rm vir}$ for the reduced sample of clusters in the AGN run at $z = 0$.

in the AGN run at $z = 0$. Since this distribution gives an idea of the location of the main shock features within and around the cluster virial region, it can be correlated with the maps of the shock Mach number distribution shown in Fig. B1. For each halo, the bumps characterizing the distribution within $R_{\rm vir}$ highlight the presence of internal shock phenomena. Outside the virial radius, most clusters show a dominant peak in the radial shock surface distribution, which approximately indicates the position of the main external accretion shock. The distributions, however, show quite irregular shapes that depend on the particular clusters' environments and evolutionary histories. Although usually it is not possible to clearly distinguish the radius for the accretion shock (see, for instance, region D3), on average, we find the external accretion shock at a mean distance of $\sim 2.5 \times R_{\rm vir}$ from the cluster centre, a value a bit larger than the results presented in previous studies (e.g. Schaal & Springel 2015; Nelson et al. 2016; Schaal et al. 2016). As discussed in Section 3.1, the height of the external peaks in the radial shock surface distribution shows some dependence on cluster mass. In this case, leaving aside some unavoidable deviations resulting from the particular clusters' evolution, the height of the distributions is clearly larger in two of the most massive systems in our sample, i.e. *D*6 and *D*21. As for region *D*10, although the peak of the distribution is similar to that of the smallest systems, it starts from below and, therefore, its absolute increase is also remarkably higher than for regions *D*2, *D*3, or *D*4. This result is in line with the fact that, in general, the extension of accretion shocks is larger around the most massive clusters (e.g. Miniati et al. 2000).

We now investigate the temporal evolution of different global shock-related quantities for the reduced sample of clusters. Fig. B5 shows the redshift evolution of the fraction of the computational volume hosting shocked cells (left-hand panel), the mean Mach number of all the cells hosting shocks (middle panel), and the ratio of CR energy flux over the thermal energy flux through shocked cells in each computational volume (right-hand panel). All these quantities have been computed within a box of side length equal to $8 \times R_{\rm vir}$ of the main cluster of each selected region. From the analysis of this figure, we obtain several interesting conclusions. The fraction of cells hosting shocks in the different simulated volumes slightly increases from an average value of ∼46 per cent at $z = 2$ up to a value of 55–60 per cent at $z = 0$. The mean values obtained at $z = 0$ are larger than those reported in previous studies (∼20 per cent, e.g. Vazza et al. 2009a; Planelles & Quilis 2013). However, we should keep in mind that, in comparison with a cosmological volume, we are analyzing a smaller and, therefore, a denser region around large clusters, which contributes to augment the amount of shocked cells. The mild increasing trend with decreasing redshift is in line with the results shown in Figs 1 and 2 for the complete sample of clusters as well as with the results shown in other analyses (e.g. Vazza et al. 2009a). As for the z-evolution of the mean Mach number, the mean strength of shocks shows values within $3 \lesssim \mathcal{M} \lesssim 4$ for all clusters. In most of the regions, the average Mach number tends to be slightly larger at $z = 0$ than at $z = 2$. In this regard, region *D*21, whose main central cluster was classified as a dynamically relaxed system, shows the lowest global variation between the high-z and the final Mach number values. According to the z-evolution of the $F_{\rm CR}/F_{\rm th}$ ratio, leaving aside some particular deviations, the mean amount of energy allocated for CR acceleration seems to be larger at higher redshift

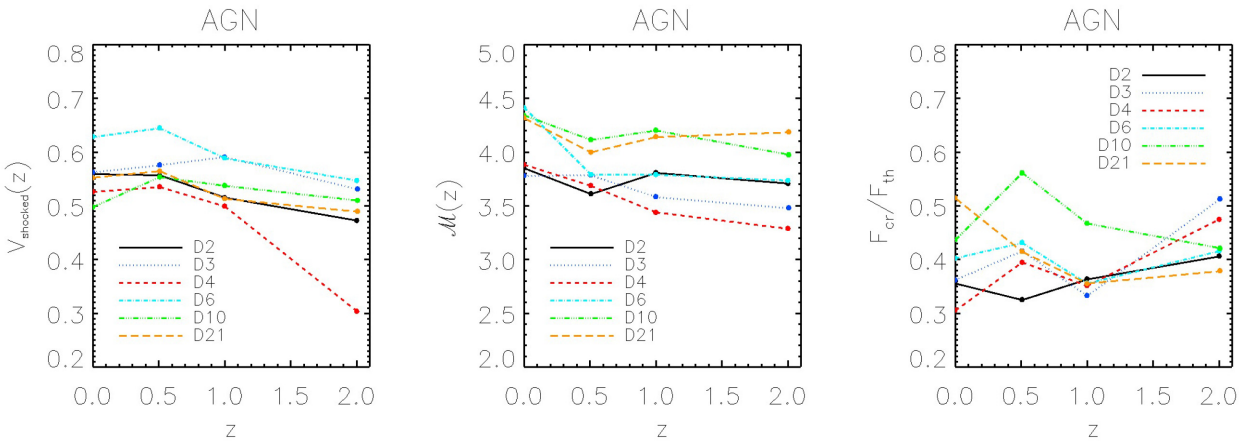


Figure B5. Redshift evolution of different global shock-related quantities within the computational domains associated to the six selected regions D2, D3, D4, D6, D10, and D21. From left to right: (i) redshift evolution of the fraction of the computational volume hosting shocked cells; (ii) redshift evolution of the mean Mach number of all the shocked cells; and (iii) redshift evolution of the ratio of CR energy flux over the thermal energy flux through shocked cells in each computational volume.

Downloaded from https://academic.oup.com/mnras/article/507/4/5703/6359160 by Universita' di Trieste user on 13 April 2022

and to slightly decrease with time. In all regions, on average, the ratio of the CR over the thermal energy flux is around ∼0.4. At the present epoch we find a value of $F_{\rm CR}/F_{\rm th}$ within ∼0.3–0.5, in line with the values obtained in previous analyses (e.g. within ∼0.1–0.35 in Vazza et al. 2009a, depending on the adopted model of energy dissipation and on the considered environment). Although the approximation employed to estimate $F_{\rm CR}/F_{\rm th}$ in post-processing is reasonable, we should keep in mind that this is a simplified treatment of the energy dissipation at shocks. Indeed, the fact that $F_{\rm CR}/F_{\rm th}$ shows larger values at early cosmic epochs claims for the need to properly, and self-consistently, solve the dynamics of the CR population and to account for its effects on the thermal distribution of the IGM (e.g. Pfrommer et al. 2006, 2007; Pfrommer et al. 2008; Vazza et al. 2016). This analysis is, however, beyond the scope of the present work.

APPENDIX C: DEPENDENCE ON BARYONIC PHYSICS

In this appendix, we explore the effect of different prescriptions for the physics of baryons on the shock cell distribution. In particular, we compare the distribution of Mach numbers at $z = 0$ for the region associated to the most massive cluster in our sample, i.e. region D21, as obtained from the NR, CSF, and AGN simulations.

Figs C1 and C2 show, respectively, 2D zoom projections of the gas overdensity and the Mach number distribution within the whole considered volume and within the virial radius of cluster D21 in the NR, CSF and AGN simulations at $z = 0$. Independently of the considered region, although the density distributions of all three runs are quite similar, both radiative runs show a larger number of small density peaks, which are mainly associated to radiative cooling and star formation processes. However, the action of AGN feedback dilutes some of these clumps and generates a much puffier density distribution than in the CSF run (see also Planelles et al. 2014). This effect is more clearly distinguishable in the upper panel of Fig. C2.

As already anticipated in Section 3.1, Fig. C1 shows that the large-scale shock cell distribution obtained for region D21 is very similar in all three runs. This behaviour was expected, since shocks in cluster outskirts are mainly driven by gravitational effects associated to cosmic structure formation processes. However, as shown in the lower panels of Fig. C2, some differences in the distribution of shocks obtained in the NR, CSF, and AGN simulations are detectable within the cluster virial region (e.g. Vazza et al. 2013; Schaal et al. 2016). Although in this particular case these differences are relatively minor, they result from the different radiative and feedback processes included in our simulations. This behaviour is also displayed in the Mach number radial profiles shown in the left-hand panel of Fig. C3.

For the sake of completeness, the right-hand panel of Fig. C3 shows the shock cell distribution function within a volume of side length equal $8 \times R_{\rm vir}$ around the centre of cluster D21 as obtained in the NR, CSF, and AGN simulations at $z = 0$. As already discussed in previous studies (e.g. Vazza et al. 2013), we find a small shortage of shocks in the AGN simulation, especially within $4 \lesssim \mathcal{M} \lesssim 60$. This difference is particularly significant between the AGN and the NR simulations: on average, AGN feedback tends to increase the mean ICM temperature, thus affecting the sound speed in the medium and, therefore, decreasing the corresponding strength of shocks. This discrepancy is similarly present when comparing the CSF and the NR simulations. Overall, these results suggest that the inclusion of radiative cooling, which removes some gas from the diffuse accretion, plays the main role, while the effect of changing the feedback prescription, namely including or not AGN feedback, is rather minor.

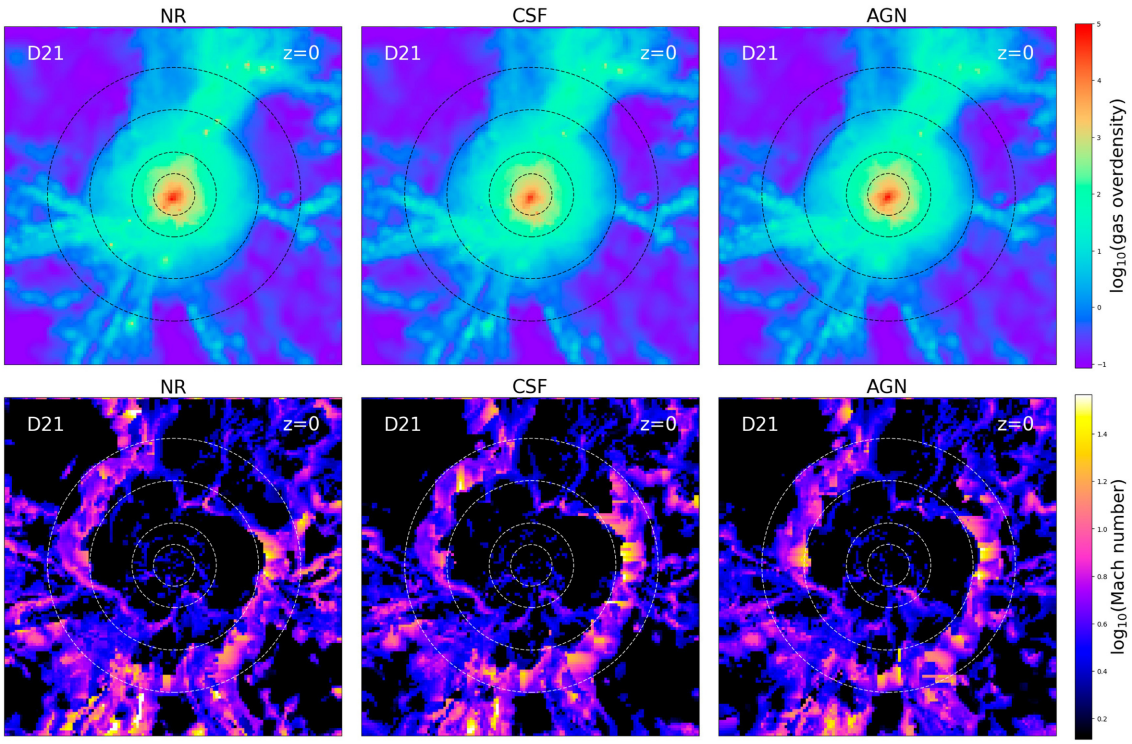


Figure C1. 2D zoom projections of the gas overdensity (upper panels) and the Mach number distribution (lower panels) around cluster D21 at $z = 0$. Panels from left to right show the maps obtained for the NR, CSF, and AGN simulations, respectively. Each map, projected along the z-axis, represents the whole region of side length equal to $8 \times R_{\rm vir}$. Circles on the maps represent R_{500}, $R_{\rm vir}$, $2 \times R_{\rm vir}$, and $3 \times R_{\rm vir}$ of the central system.

Downloaded from https://academic.oup.com/mnras/article/507/4/5703/6359160 by Universita' di Trieste user on 13 April 2022

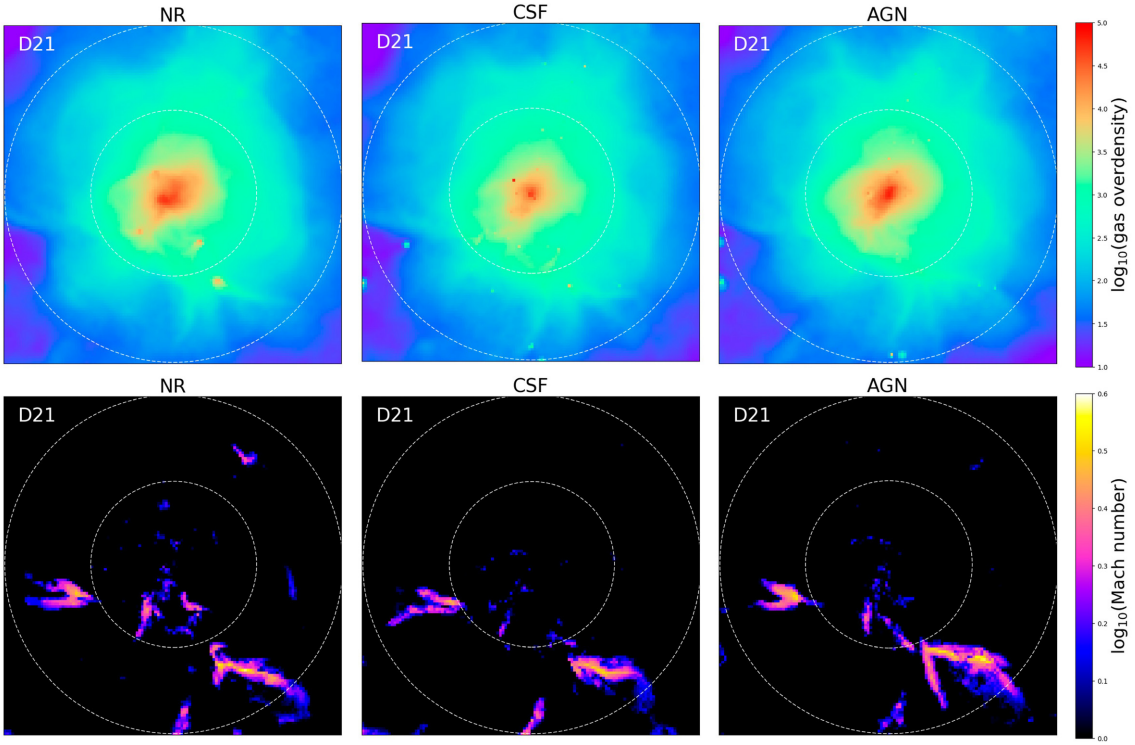


Figure C2. 2D zoom projections of the gas overdensity (upper panels) and the Mach number distribution (lower panels) around cluster D21 at $z = 0$. Panels from left to right show the maps obtained for the NR, CSF, and AGN simulations, respectively. Each map, projected along the z-axis, represents a zoom of the cluster virial region. Circles on the maps represent R_{500} and $R_{\rm vir}$ of the central system. These maps are obtained for a grid resolution corresponding to 512^3 cells.

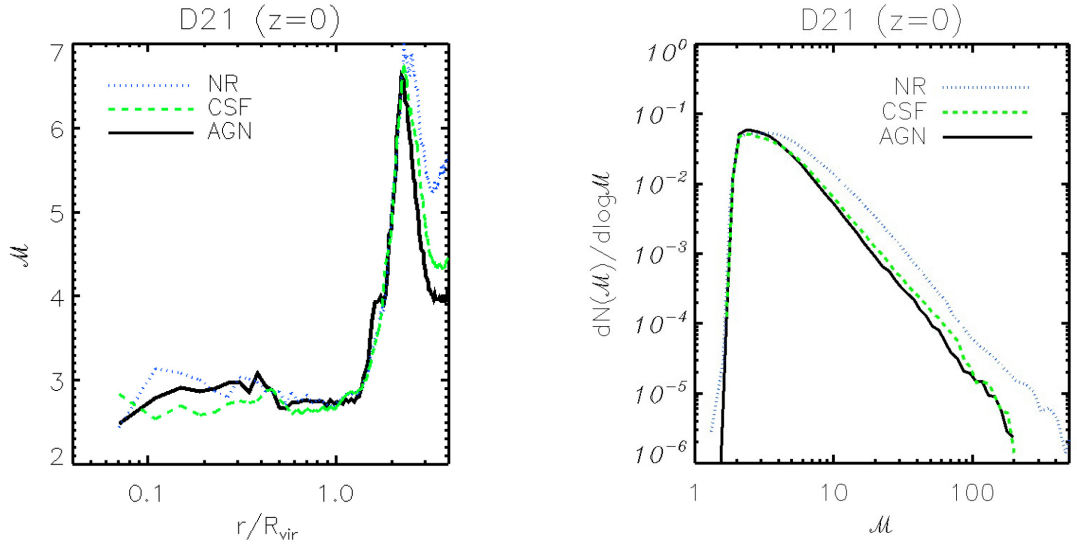


Figure C3. Left-hand panel: Volume-averaged radial profiles of the mean Mach number for the main central cluster of region D21 as obtained from the NR, CSF, and AGN simulations at $z = 0$. Right-hand panel: Shock cell distribution function within the region D21 as obtained from the NR, CSF, and AGN simulations at $z = 0$.

This paper has been typeset from a TEX/LATEX file prepared by the author.

Downloaded from https://academic.oup.com/mnras/article/507/4/5703/6359160 by Universita' di Trieste user on 13 April 2022